A Photometric Investigation of the Major Uranian Satellites

by

Abigail M. Colclasure

Submitted to the Department of Earth, Atmospheric, and Planetary Sciences
in partial fulfillment of the requirements for the degree of

Bachelor of Science in Earth, Atmospheric, and Planetary Sciences

at the

MASSACHUSETTS INSTITUTE OF TECHNOLOGY

May 2024

Author .....
Department of Earth, Atmospheric, and Planetary Sciences
May 10, 2024

Certified by .....
Dr. Michael J. Person
Senior Lecturer, Dept. of Earth, Atmospheric, and Planetary Sciences
Thesis Supervisor

Accepted by .....
Prof. Thomas Herring
Chair, Committee on Undergraduate Program

A Photometric Investigation of the Major Uranian Satellites

by

Abigail M. Colclasure

Submitted to the Department of Earth, Atmospheric, and Planetary Sciences
on May 10, 2024, in partial fulfillment of the
requirements for the degree of
Bachelor of Science in Earth, Atmospheric, and Planetary Sciences

Abstract

The Uranian system is one of the most unusual in the Solar System and its formation and evolution are poorly understood. Voyager 2 revealed that the major satellites have complex geologic features, including craters, fault systems, and chasmata. The Uranian system has been understudied and current knowledge is limit by a lack of data. The 2023-2032 decadal survey ranked a flagship NASA mission to Uranus, with a required launch window of the early 2030s, as a top priority. Further study is urgently needed, both scientifically and to inform mission planning. We conducted a photometric study, primarily using MIT's Wallace Astrophysical Observatory, and report the lightcurves of Titania and Oberon in the Sloan g', r', and i' filters. Further observations from larger telescopes are needed, but these data may indicate that ice on both Titania and Oberon has redistributed since the Voyager epoch.

Thesis Supervisor: Dr. Michael J. Person
Title: Senior Lecturer, Dept. of Earth, Atmospheric, and Planetary Sciences

Acknowledgments

I'd like to thank my advisor, Dr. Michael Person, for his guidance and support.

I'd also like to thank Timothy Brothers, the Observatory Manager at MIT's Wallace Astrophysical Observatory for his assistance with the observing efforts. I am especially grateful for the data he provided using the automated Elliot telescope.

Jane Abbott, who has helped me become a more coherent writer and presenter.

Prof. Richard Binzel, for his continued encouragement and advice.

And my fellow EAPS seniors and friends, for going on this crazy ride with me.

This work has also made use of several python packages, including, Astropy (Astropy Collaboration et al. 2022), PhotUtils (Bradley et al. 2023), the Matplotlib library (Hunter 2007), the SciPy library (Virtanen et al. 2020), the NumPy library (Harris et al. 2020), and the Pandas library (team 2020). It also made use of the VizieR catalogue access tool, CDS, Strasbourg, France, and the APASS catalog (Henden et al. 2016).

Contents

Acknowledgments **3**

1 Background and Previous Work **10**

1.1 Background . . . 10

1.2 Literature Review . . . 10

1.3 Introduction . . . 11

2 Summary of Observations **14**

3 Data Calibration **18**

4 Photometry **19**

4.1 Selection of Calibration Stars . . . 19

4.2 Centroiding . . . 19

4.3 Background subtraction . . . 20

4.4 Avoiding Diffraction Spikes . . . 21

4.5 Aperture Photometry . . . 22

4.5.1 Selection of Aperture Size . . . 23

4.5.2 Error Bars . . . 24

4.5.3 Exclusion of data . . . 24

4.5.4 Rationale for Aperture Photometry . . . 24

4.6 Phase Correction . . . 25

4.6.1 Outlier Rejection . . . 25

4.6.2 Lightcurve Folding . . . 26

5 Lightcurves **29**

6 Model Fitting **32**

6.1 Linear Models . . . 32

6.2 Periodic Models . . . 33

7 Discussion **40**

8 Conclusion **43**

8.1 Future Work 43

8.2 Broader Implications 43

9 Appendix **45**

List of Figures

1-1 Johnson V filter lightcurves of Titania and Oberon, reproduced from (Goguen, Hammel, and Brown 1989). The data in both lightcurves span about 0.2 magnitudes. It is difficult to identify a periodic trend in Titania's lightcurve, but Oberon is brightest when the Fraction of Period is between 0.4 and 0.7. 11

1-2 Phasecurves of Titania and Oberon, reproduced from (Avramchuk, Rosenbush, and Bul'Ba 2007). The plots show relative intensity as a function of phase angle. Only phase angles less than 3° are accessible from Earth. The other measurements are from Voyager 2 data. 12

1-3 Images of Titania (upper) and Oberon (lower) taken by the Voyager2 spacecraft. The magnitude of the moons is non-uniform and there are clearly identifiable brighter and dimmer patches. These are the highest resolution images ever taken of these moons. Due to Uranus's axial tilt, only the southern hemispheres of each moon could be imaged. 13

2-1 A sample image from the Carlos Sanchez Telescope taken on January 14, 2024 in the Sloan r' filter. This image demonstrates some of the challenges associated with these observations, namely the saturation and diffraction spikes from Uranus. 15

4-1 The error and ellipiticty of the centroids, plotted both as a function of the data of observation and as histograms. The error reported here is the quadrature sum of the x and y error of the 2D Gaussian fit to the source. The centroid error from both the calibration stars and the moons is shown. A smaller error indicates that the source has a smaller point spread function and that it could be easier to resolve the moons from Uranus. Here, the ellipticty is defined as the ratio the x and y standard deviations. If the PSF is perfectly circular, the ellipticity should be 1. 21

4-2 Example point spread functions from 01/14/2024 observations with the Carlos Sanchez telescope. The PSFs are non-Gaussian and variable over the course of the night. Because of this variation, PSF and differential photometry are difficult and require that different models be fit to each image. 22
4-3 2D Gaussian fit of Artemis data from 01/16/2024. The residuals indicate that the PSF is non-Gaussian. Similarly to the Carlos Sanchez telescope data the shapes of the PSFs make PSF and differential photometry difficult. 22
4-4 The angle between Uranus and Titania (left) and Uranus and Oberon (right) is plotted as a function of the observation date. This angle was computed between the moons sometimes landed in one of Uranus's diffraction spikes. In all of the data, except for the TCS, the diffaction spikes were at 0°, 90°, 180°, and 270°. For the TCS, the diffraction spikes were at 45°, 135°, 225°, and 315°. Images where the moon was within 15° of a diffraction spike were excluded from the lightcurves. 23
4-5 Titania (left) and Oberon (right) in the g' filter 27
4-6 Titania (left) and Oberon (right) in the r' filter 27
4-7 Titania (left) and Oberon (right) in the i' filter 27
4-8 Signal-to-Noise ratio as a function of aperture radius size. Each line on the graph represents a different night of data. To make the graphs more readable, only every third night is shown. For a given night's data, the relative flux of the target in each image was measured for a variety of aperture sizes. These aperture sizes were 0.5, 1.0, 1.5, 2.0, 2.5, 3.0, and 3.5 times the median of the quadrature sum of the target's centroid standard deviations. No aperture radii that were smaller than 1 pixel were considered. Then, the aperture radius that resulted in the highest signal-to-noise ratio was selected. For display purposes, the aperture radii and SNR for each night are normalized to be between 0 and 1. As a function of aperture radius, the signal-to-noise ratio should increase, reach a peak, and then decrease. Notice that only some of the lines follow this trend. 27
4-9 All data, regardless of the filter or target, was used to create a single phasecurve. This phasecurve was used to correct the lightcurves for the apparent change in magnitude as the distance between the Earth and Uranus changes. 28

5-1 Titania's lightcurve in the Sloan g' filter 29
5-2 Titania's lightcurve in the Sloan r' filter 30
5-3 Titania's lightcurve in the Sloan i' filter 30
5-4 Oberon's lightcurve in the Sloan g' filter 30
5-5 Oberon's lightcurve in the Sloan r' filter 31
5-6 Oberon's lightcurve in the Sloan i' filter 31

6-1 Best-fit horizontal line for Titania's g' lightcurve. The mean of the residuals from longtiude 75° - 275° is 0.183 magnitudes whereas the mean of the residuals from longitude 275° - 75° is -0.21 magnitudes. These differences indicate that Titania is not uniformly bright. 32
6-2 Best-fit horizontal line for Oberon's i' lightcurve. The mean of the residuals from longitude 25° - 300° is -0.11 magnitudes whereas the mean of the residuals from longitude 300° - 25° is 0.02 magnitudes. These differences indicate that Oberon is not uniformly bright. 33
6-3 Periodic Models for Titania's g' lightcurve 36
6-4 Periodic Models for Titania's r' lightcurve 37
6-5 Periodic Models for Titania's i' lightcurve 37
6-6 Periodic Models for Oberon's g' lightcurve 38
6-7 Periodic Models for Oberon's r' lightcurve 38
6-8 Periodic Models for Oberon's i' lightcurve 39
6-9 The reduced χ^2 as a function of Fourier transform order for each of the model lightcurves. A sharp change in the slope of the line could indicate the optimal order, but many of the lines do not have such a feature. 39

7-1 The model Oberon's i' lightcurve subtracted from the model of Oberon's r' lightcurve 42

List of Tables

2.1 A summary of the observations made during this campaign. Data were taken in the Sloan g', r', i' and z' filters, primarily from MIT's Wallace Astrophysical Observatory. Observations began on November 1, 2023 and ended on January 17, 2024. Data on the Elliot telescope were taken by Tim Brothers using the automated observing program and all other data was taken manually. All data were taken with 1x1 binning and with CCD cameras in conventional mode. The exposure times of the images varied across filters and across nights. 17

9.1 A list of the calibration stars used for photometric analysis on each night. All information presented here reflects values reported in the APASS catalog. Three stars were selected for each image, except when there were not three stars in the field. Note that APASS reports the error bars for some of these stars as 0, but that means that the error bar is not known. The identifier column lists the APASS catalog's reference number for that star. 51

Chapter 1

Background and Previous Work

1.1 Background

The Uranian system is one of the most unusual in the Solar System and remains poorly understood. Among some of the mysteries are the cause of Uranus's 99.77° axial tilt, the effects of its strongly multi-polar magnetic field, and its atmospheric energy balance. Similarly, there is much left to discover about its satellites' formations, evolutions, compositions, and internal structures. Voyager 2 discovered 11 of the 27 known moons and delivered the highest resolution images ever taken of all five major satellites. The Voyager 2 images revealed complex geologic features on the major moons, such as craters, fault systems, and chasmata, however the causes of these features are largely unknown. Further, due to the orientation of the Uranian system, Voyager 2 only imaged the southern poles of these moons and there are no high-resolution images of their northern poles. Current knowledge is limited by a lack of data since no spacecraft has returned since Voyager 2's flyby in 1986. As such, the 2023-2032 decadal survey ranked a flagship NASA mission to Uranus as a top priority. With a required launch window of the early 2030s, there is an urgent need for further investigation of Uranian system, both from a scientific perspective and to inform space mission planning.

1.2 Literature Review

While lower-resolution than spacecraft images, the surface properties of the Uranian satellites can be studied photometrically and spectroscopically using ground-based telescopes. Measurements have been made before, such as by (Avramchuk, Rosenbush, and Bul'Ba 2007), (R. J. Cartwright et al. 2015), and (Detre et al. 2020), but continuing observations can further advance our science interpretation of their surfaces in advance of their forthcoming spacecraft exploration. These works, respectively, compiled all photometric data available in the literature to construct phasecurves of

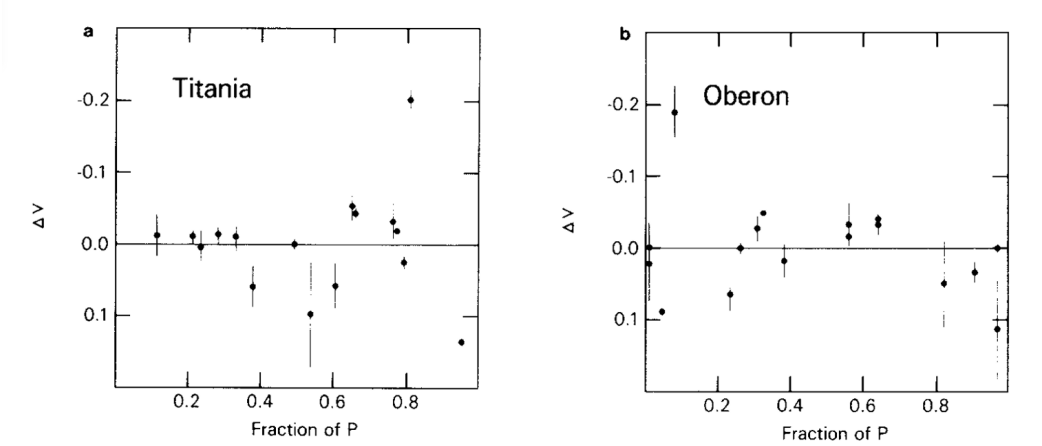

Figure 1-1: Johnson V filter lightcurves of Titania and Oberon, reproduced from (Goguen, Hammel, and Brown 1989). The data in both lightcurves span about 0.2 magnitudes. It is difficult to identify a periodic trend in Titania's lightcurve, but Oberon is brightest when the Fraction of Period is between 0.4 and 0.7.

the major satellites for the phase-angle interval 0.034° – 35°, made spectrophotometric measure from 0.81 to 2.42 micrometers, and made photometric measurements in the far infrared. Ground-based observations have also identified several specific features which merit investigation. For example, spectral measurements have revealed H2O and CO2 ices on all the major moons, except for Miranda which lacks evidence for CO2 ice (DeColibus, Chanover, and Richard J. Cartwright 2023). Interestingly, the ices are not evenly distributed on the leading and trailing hemispheres of the moons; H20 ice absorption features are more prominent on the leading hemispheres of Ariel, Umbriel, and Titania, but on the trailing hemisphere of Oberon (Grundy et al. 2006). It is hypothesized that the asymmetry on the hemispheres is due to electron bombardment resulting from Uranus's magnetic field, but the cause of the discrepancy in ice distribution on the different moons is not yet known. Another feature of interest is the localized spot of red dust found on Titania's leading hemisphere (Richard J. Cartwright, Emery, et al. 2018). While these data suggest that the red dust infalls from the outer, irregular satellites, it was also noted that additional observations in visible and near infrared wavelengths could provide key insight into the extent of the spot. Therefore, even though they have provided key insights, measurements such as these have yet to cover the whole range of wavelengths and phase angles.

1.3 Introduction

The lack of up-to-date full rotational lightcurves of these objects limits our understanding of their surface properties. The major satellites are all tidally locked with rotation periods ranging from 1.4 – 13.5 days, so high-time resolution lightcurves can be obtained without an unreasonably extensive

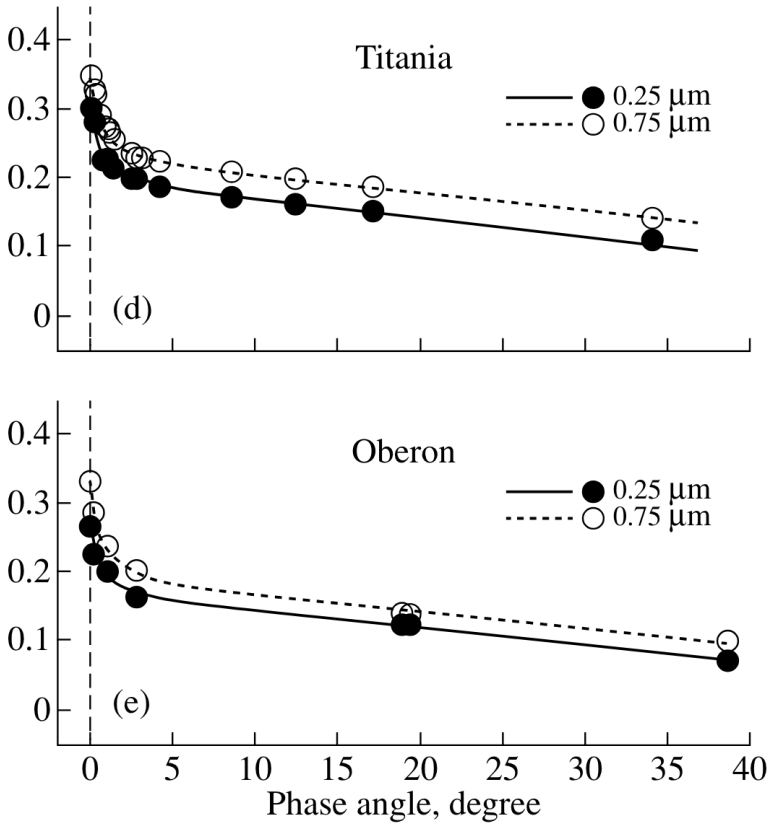

Figure 1-2: Phasecurves of Titania and Oberon, reproduced from (Avramchuk, Rosenbush, and Bul'Ba 2007). The plots show relative intensity as a function of phase angle. Only phase angles less than 3° are accessible from Earth. The other measurements are from Voyager 2 data.

Figure 1-3: Images of Titania (upper) and Oberon (lower) taken by the Voyager2 spacecraft. The magnitude of the moons is non-uniform and there are clearly identifiable brighter and dimmer patches. These are the highest resolution images ever taken of these moons. Due to Uranus's axial tilt, only the southern hemispheres of each moon could be imaged.

observing campaign. Lightcurves of the satellites Titania and Oberon in the Sloan g', r', and i' filters are reported here. Titania and Oberon were selected as the targets of interest because these two satellites are the brightest and the farthest away from Uranus. Because observations were primarily made with 14 and 24 inch telescopes, it was difficult to resolve the inner satellites from Uranus. In addition to being more easily resolved, Titania and Oberon were less impacted by contamination due to Uranus's saturation and diffraction spikes.

Chapter 2

Summary of Observations

Observations were taken from November 2023 through January 2024 and primarily made at MIT's Wallace Astrophysical Observatory. Three nights of data were also collected at Teide Observatory in Tenerife, Spain. As summarized in table 2.1, observations at Wallace Observatory were made using the Pier 2, Pier 3, and Elliot telescopes and observations at Teide Observatory were made using the Carlos Sanchez and Artemis telescopes. Pier 2 and Pier 3 are 14 inches in diameter, the Elliot is 24 inches in diameter, the Carlos Sanchez is 1.52 meters in diameter and Artemis is 1 meter in diameter.

Data on the Elliot telescope were taken by Tim Brothers using the automated observing program and all other data was taken manually. All data were taken with 1x1 binning and with CCD cameras in conventional mode. 1x1 binning was selected to better resolve the moons from Uranus. Conventional mode, as opposed to electron amplifying mode, was chosen because the dynamic range of the camera was more important than the sensitivity to light. The primary challenge of these observations is that the moons are much fainter than and relatively close to Uranus. Additionally, the observations did not need to be taken with high temporal resolution. Since the periods of Titania and Oberon are 8.807 and 13.43 days respectively, using an electron amplifying mode to shorten the exposure time was unnecessary and the amplified noise was undesirable.

With the exception of Pier 2, all data were taken in the Sloan g', r', i', and z' filters. In addition to the Sloan filters, data on Pier 2 were collected in the Johnson V filter. The Johnson filter was selected because previously published lightcurves of Titania and Oberon were only taken in the V filter. Uranus was at opposition on November 13, 2023 with a transit altitude of 65°. From January 14 - January 21, 2024 when observations were made at Teide Observatory, Uranus transited at an altitude of almost 80°. Observations taken at a higher altitude are preferable because there is a lower airmass. When there is a large airmass, the light passes through more of the Earth's atmosphere and there is more extinction. When possible, observations were taken within 2 hours of Uranus transiting.

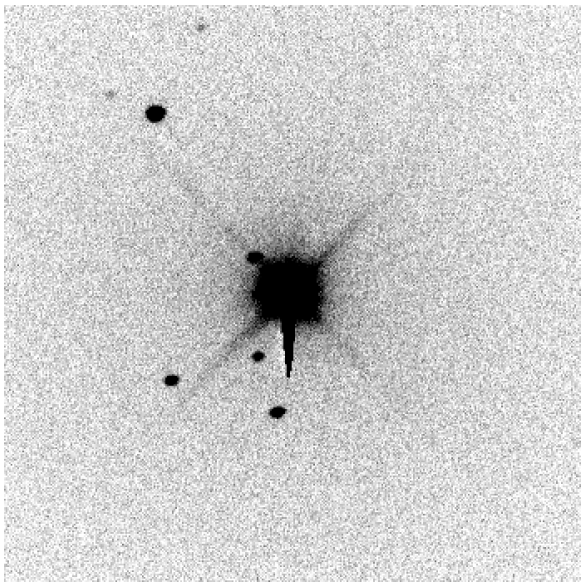

Figure 2-1: A sample image from the Carlos Sanchez Telescope taken on January 14, 2024 in the Sloan r' filter. This image demonstrates some of the challenges associated with these observations, namely the saturation and diffraction spikes from Uranus.

At transit, Uranus reaches the highest altitude it will during a given night. Observations centered at the transit time were not always possible due to weather and to accommodate other observing programs. Observations are also more ideal during opposition. At opposition, the distance between the Earth and Uranus is the smallest, so Uranus and the moons appear brighter.

Exposure times ranged from 2 seconds to 120 seconds. Shorter exposure times were used for the g', r', and V filters and longer exposure times were used for the i' and z' filters because Uranus is brighter in the g', r' and V wavelengths than the i' and z' wavelengths. The PSF is independent of the exposure time, but it was important to ensure that Uranus was not saturated. If Uranus was saturated, then it would be impossible to model Uranus's PSF and perform differential photometry. However, a shorter exposure time could result in a relatively larger contribution from read noise. The read noise of the CCD is independent of the exposure time, so a shorter exposure time with fewer counts in the image could make the read noise relatively higher. The exposure times varied within a night and across nights due to changing weather conditions. It is worth noting that simultaneous data in multiple filters on the TCS could only be acquired with exposure times of 2 seconds or longer. With a 2 second exposure time, it was difficult to resolve the inner major satellites from Uranus in the r' and g' filters due to saturation.

Uranus has magnitudes of -7.11, -6.97, -6.82, -5.76, -4.91 in V, g', r', i', and z' respectively (Mallama, Krobusek, and Pavlov 2017). Observations were more challenging in filters where Uranus was brighter. The moons are also brighter in the filters where Uranus is brighter, but it was more difficult to avoid saturation. A sample image from the Carlos Sanchez Telescope taken on January

14, 2024 in the r' filter is provided in this chapter. This image demonstrates some of the challenges associated with these observations, namely the saturation and diffraction spikes from Uranus. A discussion of how these challenges were addressed during the photometric analysis is given in chapter 4.

Telescope Name	Observatory	Diameter	Instrument	Plate Scale (“/pixel)	Field of View (arcmin)	Number of Observations
Pier 2	Wallace	14 in	SBIG STL-1001e CCD	1.208	20.6’ x 20.6’	5
Pier 3	Wallace	14 in	FLI ML1001 CCD	1.189	20.3’ x 20.3’	5
Elliot	Wallace	24 in	FLI PL16803 CCD	0.47	32’ x 32’	24
Carlos Sanchez	Teide	1.52 m	Muscat2	0.434 (g’)	7.41’ x 7.41’ (g’)	2
				0.434 (r’)	7.41’ x 7.41’ (r’)	
				0.435 (i’)	7.43’ x 7.43’ (i’)	
Artemis	Teide	1 m	Andor15 iKon-L CCD (BEX2-DD-9TW)	0.35	12’ x 12’	1

Table 2.1: A summary of the observations made during this campaign. Data were taken in the Sloan g’, r’, i’ and z’ filters, primarily from MIT’s Wallace Astrophysical Observatory. Observations began on November 1, 2023 and ended on January 17, 2024. Data on the Elliot telescope were taken by Tim Brothers using the automated observing program and all other data was taken manually. All data were taken with 1x1 binning and with CCD cameras in conventional mode. The exposure times of the images varied across filters and across nights.

Chapter 3

Data Calibration

All data were dark subtracted and flat corrected. Dark and flat images are used to minimize noise due to systematic effects from the camera and optics. Dark images are important for minimizing readout noise and thermal noise in the camera. Dark images were taken at the same temperature and exposure time as the data. At minimum, 3 dark images were taken at each temperature and exposure time. The dark images were median combined to create a master dark image. The master dark image was subtracted from each of the science images.

Flats are important to minimize the effects of vignetting and correct for the effects of dust present in the optical system. Flat images were taken at twilight with the telescope pointed due east and at 45° altitude and with the telescope's tracking turned off. Pointing the telescope away from the setting sun allows for the most uniform sky conditions. Turning the tracking off ensures that any stars in the images will leave trails as opposed to remaining centered on the same pixel. This means that when the flat images are median combined to create a master flat, any stars will be removed. They were also taken in each of the filters that data were taken in because the vignetting and dust can be significantly different in different wavelengths. One set of flat images were taken and used for each night in the data set. Before being median combined to create a master flat, each flat image had a bias imaged subtracted from it and was normalized by dividing by the median of the counts in each pixel in that image. Flats measure how uniform the CCD pixels sensitivity are, so the relative values across an image matter more than the absolute number of counts in each pixel. Each science image was divided by the master flat after being dark corrected.

Chapter 4

Photometry

Photometry of the satellites was complicated because the moons are relatively faint, around magnitude 14, and located near a bright, magnitude 5, planet. To complete photometry, several steps needed to be taken. First, comparison stars needed to be identified in each image. Second, the positions of the reference stars and the target needed to be measured. Finally, the relative brightness of the moons needed to measured, with respect to the reference stars.

4.1 Selection of Calibration Stars

Calibration stars are necessary to measure the absolute brightness of the moons and to minimize error due to extinction from Earth's atmosphere. Calibration stars with known magnitudes were selected for each night. These comparison stars were chosen because they had g', r', and i' magnitudes listed in the APASS catalog. No stars with known z' magnitudes were in the field of view on any night. Three stars were selected for each image, except when there were not three stars in the field with Sloan magnitudes reported in APASS. A list of the calibration stars chosen for each night is given in table 9.1. Calibration stars were selected from the APASS catalog because it reports Sloan magnitudes. APASS reports the error bars for some of these stars as 0, but that means that the error bar is not known. Calibration stars are more ideal if they are located near Uranus, have similar magnitudes to the moons, and can be used on multiple nights of observations. It is also preferred for the calibration stars to be located on different stars of Uranus so that they can account for the differences in atmospheric extinction in different parts of the sky.

4.2 Centroiding

Centroiding on the targets and comparison stars was done with a version of the Python PhotUtils centroids package modified for this project. Both the 2D Gaussian and quadratic centroiding

feautres were used, but the 2D Gaussian function was modified so that it would also return the standard deviation of the best-fit Gaussian in addition to the mean. Both the Gaussian and quadratic PhotUtils centroiding functions find the best fit function for a rectangular subframe of the image. A guess of the location of the target in the first image was manually identified. For subsequent images, the centroid from the previous image was used as an initial guess for the centroid. In cases where the target abruptly moved, this process was repeated in the middle of the image series. In each image, the centroid function was called twice. The first had the function was called, a larger portion of the image was subframed. This was to allow for the target to move farther between images. Then a smaller region, centered on the centroid from the larger subframe, was used. The centroid from this smaller region was taken as the final centroid. The first centroid with the larger subframe sometimes used the Gaussian function and sometimes used the quadratic function, depending on which one enabled the fitter to successfully produce a model. The second centroid with the smaller subframe always used the Gaussian model. The standard deviations from this model were taken was the error bars on the centroid. The PhotUtils Gaussian centroid function expects that the data is already background subtracted. Before fitting the centroids, the subframe of the data that would be fitted was background subtracted, in the way described in section 4.3. The centroids were visually inspected the ensure that this process was successful. The centroid error is shown in figure 4-1. The error reported here is the quadrature sum of the x and y error of the 2D Gaussian. The centroid error from both the calibration stars and the moons is shown. A smaller error indicates that the source has a smaller point spread function. A smaller point spread function is desirable because it results in more precise photometry. It is easier to resolve the moons and Uranus when the PSF is smaller. It also increases the signal-to-noise ratio because there are fewer systematic effects due to the detector. Read noise, for example, would be decreased because there is noise from a smaller number of pixels. The ellipticity is also reported in figure 4-1. Here, the ellipticty is defined as the ratio the x and y standard deviations. If the PSF is perfectly circular, the ellipticity should be 1. A perfectly circular PSF is desirable because it indicates that the telescope is well focused and well calibrated. It is also simpler to perform photometry when the PSF is circular. Circular aperture photometry is the most straightforward version of aperture photometry and is most accurate when the PSF is circular.

4.3 Background subtraction

Background subtraction is important to correct for varying sky brightness due to atmospheric effects. Background subtraction was done using the PhotUtils background.Background2D function.

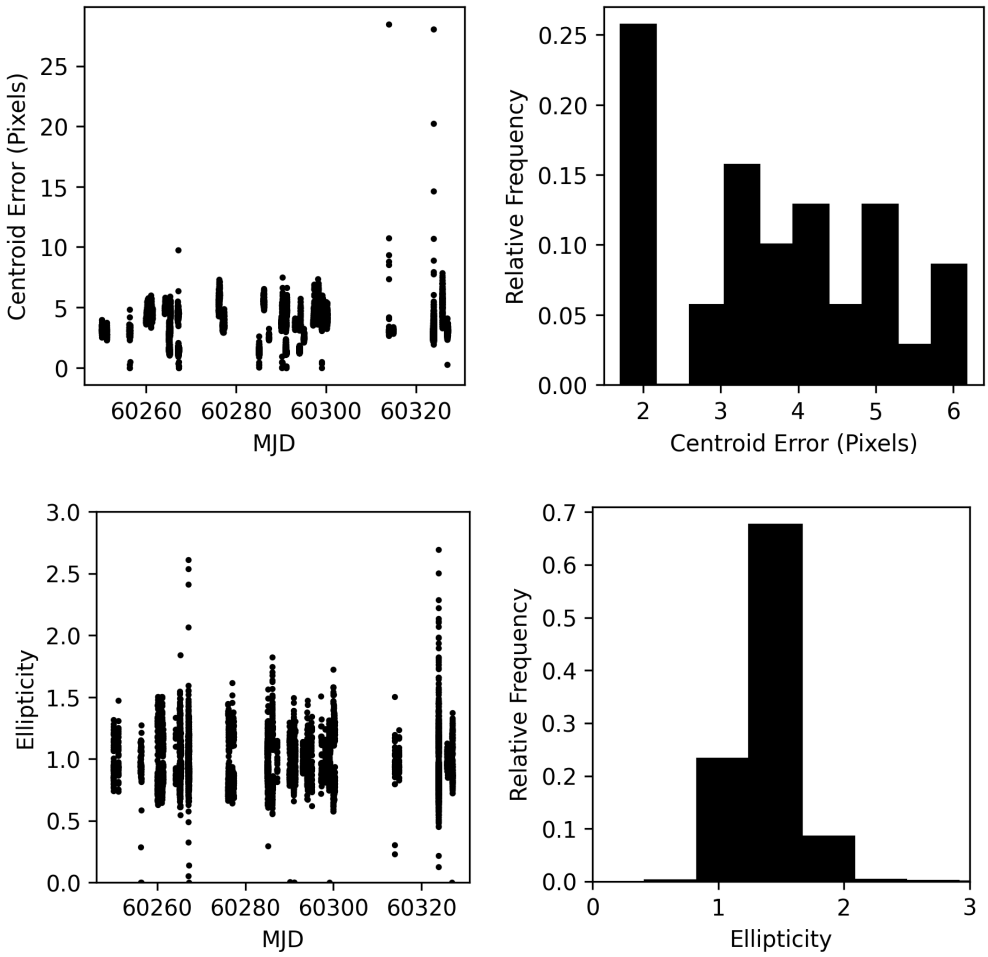

Figure 4-1: The error and ellipiticty of the centroids, plotted both as a function of the data of observation and as histograms. The error reported here is the quadrature sum of the x and y error of the 2D Gaussian fit to the source. The centroid error from both the calibration stars and the moons is shown. A smaller error indicates that the source has a smaller point spread function and that it could be easier to resolve the moons from Uranus. Here, the ellipticty is defined as the ratio the x and y standard deviations. If the PSF is perfectly circular, the ellipticity should be 1.

4.4 Avoiding Diffraction Spikes

Background subtraction often fails when a moon is in one of the diffraction spikes. The diffraction spike goes either horizontally or vertically and does not evenly surround the moon. This means that the moon appears brighter than it should. Images where a moon was within 15° of a diffraction spike were excluded from the lightcurve. The angle between the moon and Uranus was measured after measuring the pixel location of the moon and Uranus. The moons centroid was used for the location of the moon. The location of Uranus was taken as the pixel at the center of the brightest 15 x 15 pixel box in the image. Uranus is always the brightest target in the image and finding the center of this box was more straightforward than centroiding. Fitting a Gaussian of quadratic

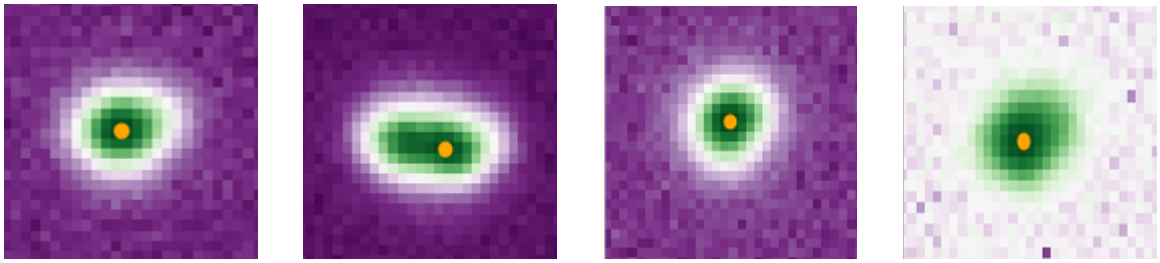

Figure 4-2: Example point spread functions from 01/14/2024 observations with the Carlos Sanchez telescope. The PSFs are non-Gaussian and variable over the course of the night. Because of this variation, PSF and differential photometry are difficult and require that different models be fit to each image.

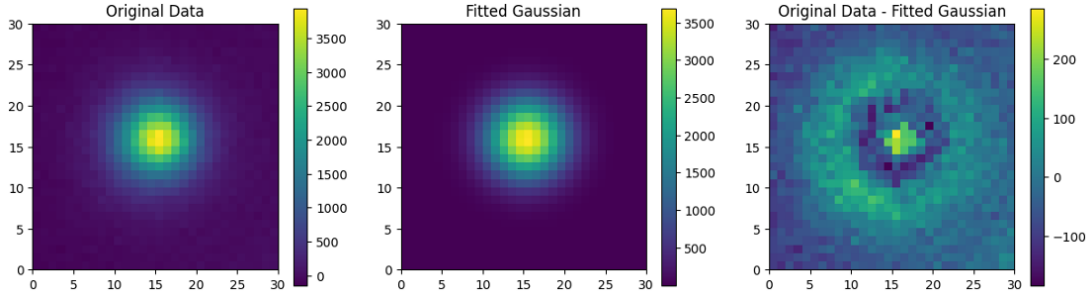

Figure 4-3: 2D Gaussian fit of Artemis data from 01/16/2024. The residuals indicate that the PSF is non-Gaussian. Similarly to the Carlos Sanchez telescope data the shapes of the PSFs make PSF and differential photometry difficult.

function with photutils, as described in the centroiding section would have been significantly more complicated. In all of the data, except for the TCS, the diffraction spikes were at 0°, 90°, 180°, and 270°. For the TCS, the diffraction spikes were at 45°, 135°, 225°, and 315°. The angle between the moons and Uranus is shown in figure 4-4. The data that were excluded because the moon fell on a diffraction spike could be included of the brightness of the diffraction spikes were modelled and subtracted from each image. This modelling was outside the scope of this project.

4.5 Aperture Photometry

In circular multi-aperture photometry, once the data has been properly calibrated, the brightness of the target is measured by comparing it to the brightness of the reference stars. Essentially, a circle is drawn around the centroid of each source and the number of counts inside of the aperture are summed. This ratio of the flux of the target to the reference stars is known as the relative flux. If the absolute magnitude of the reference stars are known, the relative flux of the target can be converted into an absolute magnitude. It is important that the size of the aperture for the target and the comparison stars be the same. However, the aperture size can be varied across images. It is also acceptable if Titania and Oberon have different aperture sizes so long as the aperture size used

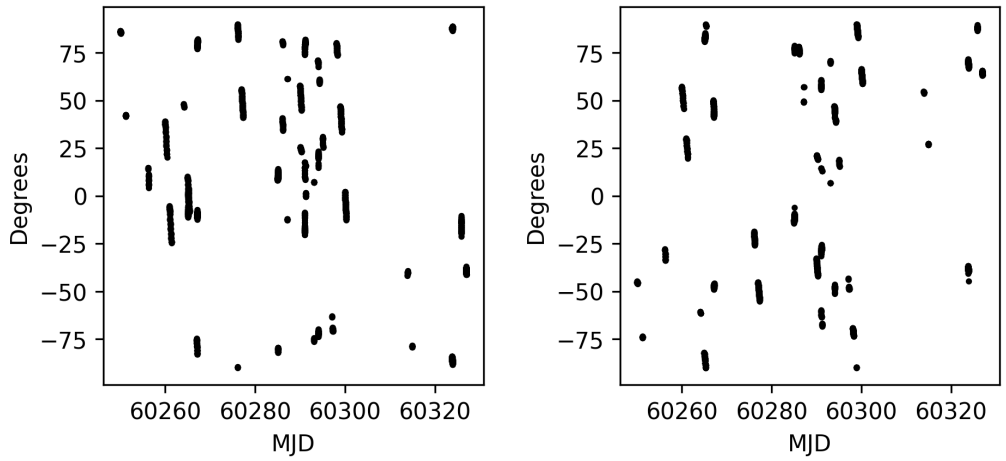

Figure 4-4: The angle between Uranus and Titania (left) and Uranus and Oberon (right) is plotted as a function of the observation date. This angle was computed between the moons sometimes landed in one of Uranus's diffraction spikes. In all of the data, except for the TCS, the diffaction spikes were at 0°, 90°, 180°, and 270°. For the TCS, the diffraction spikes were at 45°, 135°, 225°, and 315°. Images where the moon was within 15° of a diffraction spike were excluded from the lightcurves.

for the reference stars is also changed to match. Aperture photometry requires that the sources are well separated. Because counts inside of a given aperture are all summed together, there is no way of knowing how much light came from each individual source.

4.5.1 Selection of Aperture Size

For a given night's data, the relative flux of the target in each image was measured for a variety of aperture sizes. These aperture sizes were 0.5, 1.0, 1.5, 2.0, 2.5, 3.0, and 3.5 times the median of the quadrature sum of the target's centroid standard deviations. No aperture radii that were smaller than 1 pixel were considered. Then, the aperture radius that resulted in the highest signal-to-noise ratio was selected. The aperture radii was fixed for a given night. To compute the signal-to-noise ratio, it was assumed that the flux of the target should be constant over the course of the night. The signal to noise ratio was then the median of the measured relative flux of the target divided by the standard deviation of the measurements.

As a function of aperture radius, the signal-to-noise (SNR) ratio should increase, reach a peak, and then decrease. At first, the signal-to-noise ratio should grow as more of the light from the target is being capture in the radius. Eventually, as the radius continues to grow, proportionally more background light will be included than light from the source which should result in a decrease in the signal-to-noise ratio. However, in practice, the SNR curve does not always follow this trend. The SNR curves for each night are shown in figure 4-8. Selecting a different aperture radius for each image was also considered. However, many of these SNR curves looked like exponential decay functions, instead of having a maximum as described above.

4.5.2 Error Bars

The same error bar were assigned to every data point from a given night by computing the variance of the measurements for that night.

4.5.3 Exclusion of data

Data which was heavily impacted by saturation, such as the data from the Carlos Sanchez telescope were not included in the final lightcurves. Data taken in the V filter were also not processed because Uranus is brighter in the V filter and Uranus had a large PSF with lots of stray light, even when the exposure time was less than 1 second. These data could be included if other photometric techniques, such as PSF photometry or differential photometry are used. The reasons for selecting aperture photometry instead of PSF or differential photometry are outlined in section 4.5.4. Data from exceptionally poor weather nights were also not included.

4.5.4 Rationale for Aperture Photometry

Aperture photometry, PSF photometry, and differential photometry were considered. In short, circular multi-aperture photometry was ultimately selected because it was the simplest approach. The complication factors for PSF and differential photometry, as well as their benefits, are outlined in this section.

PSF Photometry

Point spread function (PSF) photometry involves modelling the PSF of the sources in the image. The measured flux of a given source is the sum of the PSF convolved with the image. Then the relative flux of the target with the reference stars is measured in the same way as in aperture photometry. PSF photometry is especially good for sources that are not completely resolved, and so could be useful given that moons are nearby Uranus. Every source in the image should have the same PSF, so one could measure the PSF on the outer moons of Titania and Oberon and then apply that PSF to get flux measurements of the inner moons, Miranda, Ariel, Umbriel. It could even be possible to measure the PSF by using a reference star which is very well separated from Uranus.

Modelling the PSFs of Titania and Oberon in the data from the Carlos Sanchez telescope was attempted. This data was selected because the Carlos Sanchez telescope had the largest diameter and largest angular resolution. To perform PSF photometry, a 2D Gaussian PSF was fit to the outer moons and comparison stars in each image and then applied to the inner moons. A separate PSF was fit for each source, however, it would be preferable to perform a joint optimization to fit the same PSF to all of the sources. The PSFs were fit seperately for simplicity. It became clear that a 2D Gaussian would be insufficient to fit the PSF. In theory, the PSF should be Gaussian. Gaussian

PSFs were also fit to the Artemis data, since the PSFs appeared more Gaussina by eye than the TCS PSFs. However, there were non-Gaussian residuals after the Gaussian PSF was fit. PSF photometry with a 2D Gaussian PSF on the Artemis data produced a lightcurve where Titania and Oberon were around magnitude 11, which is illogical given that Titania and Oberon are both roughly magnitude 14. In order to do PSF photometry with any reasonable level of accuracy, a more complicated PSF is needed. A rotated 2D Gaussian is a reasonable next step, but other, non-Gaussian functions will also be needed. Additionally, the PSF does not appear to be constant over the course of one night or between telescopes. Therefore, PSF photometry will likely require several, complicated PSF models.

Differential Photometry

Differential photometry involves modelling the light from Uranus, including any saturation or diffraction spikes, and subtracting them out from the image. Similarly to PSF photometry, this can work better than aperture photometry when the sources are not completely resolved. Unfortunately, modelling the light of Uranus, the saturation, and diffraction spikes is quite involved and would require a different model in each image.

4.6 Phase Correction

Uranus was at opposition on November 13, 2023. As it gets farther away it appears dimmer. This is corrected for by modeling the phasecurve and subtracting it from the lightcurve. The lightcurves reported in chapter 5 show the ratio of the magnitude the target compared to the phasecurve. The NASA JPL Horizons software was used to retrieve the sun-target-observer angle for each night. An exponential decay function was fit to the magnitude as a function of phase angle. All data, regardless of the filter or target, was used to create a single phasecurve. Because the surfaces of the moons could have wavelength dependent scattering properties and because the surfaces of Titania and Oberon are different from each other, it would be more accurate to have separate phasecurves for each moon in each filter. Note that the phasecurve reported here provides much higher time resolution of phase angles 0° to 2° than are reported in (Avramchuk, Rosenbush, and Bul'Ba 2007). Only phase angles from 0° to 3° are accessible with ground based observations.

4.6.1 Outlier Rejection

Once the lightcurves were produced, data points that were farther than 3 standard deviations away from the median of all the data points were excluded.

4.6.2 Lightcurve Folding

The period of Titania and Oberon are known and reported by NASA JPL Horizons as 8.706 days and 13.46 days respectively. To fold the lightcurves, the magnitude is determined as a function of each moon's longitudal phase. The longitudinal phase was computed for each image using the MJD of the observations and the observer sub-longitude reported by the NASA JPL Horizons software.

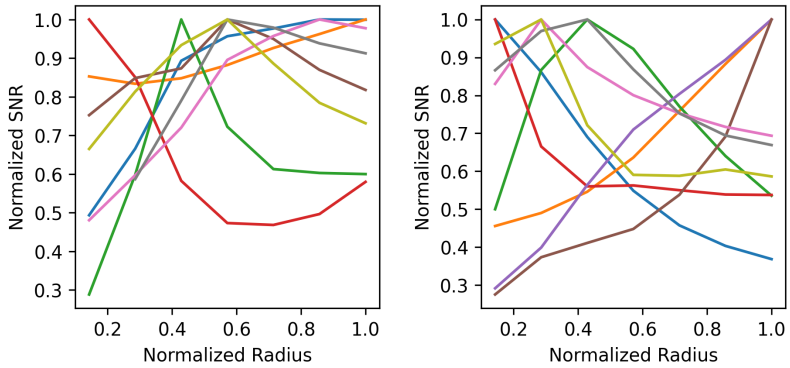

Figure 4-5: Titania (left) and Oberon (right) in the g' filter

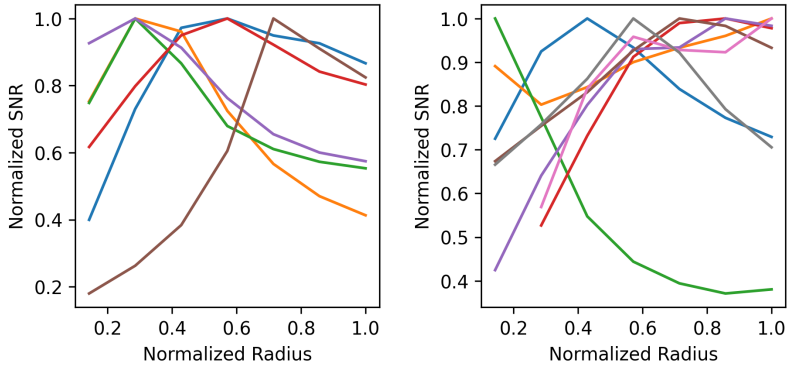

Figure 4-6: Titania (left) and Oberon (right) in the r' filter

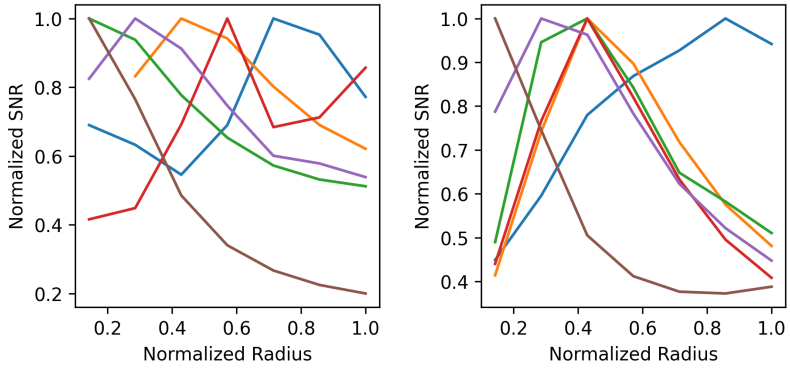

Figure 4-7: Titania (left) and Oberon (right) in the i' filter

Figure 4-8: Signal-to-Noise ratio as a function of aperture radius size. Each line on the graph represents a different night of data. To make the graphs more readable, only every third night is shown. For a given night's data, the relative flux of the target in each image was measured for a variety of aperture sizes. These aperture sizes were 0.5, 1.0, 1.5, 2.0, 2.5, 3.0, and 3.5 times the median of the quadrature sum of the target's centroid standard deviations. No aperture radii that were smaller than 1 pixel were considered. Then, the aperture radius that resulted in the highest signal-to-noise ratio was selected. For display purposes, the aperture radii and SNR for each night are normalized to be between 0 and 1. As a function of aperture radius, the signal-to-noise ratio should increase, reach a peak, and then decrease. Notice that only some of the lines follow this trend.

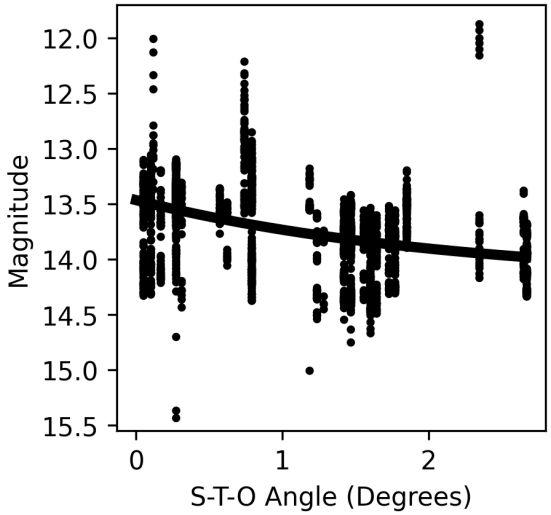

Figure 4-9: All data, regardless of the filter or target, was used to create a single phasecurve. This phasecurve was used to correct the lightcurves for the apparent change in magnitude as the distance between the Earth and Uranus changes.

Chapter 5

Lightcurves

Lightcurves of Titania and Oberon were measured in the Sloan g', r', and i' filters in the way described in chapter 4. They are plotted as the magnitude relative to the phasecurve as a function of the moon's longitudinal phase. The longitudinal phase was determined as described in section 4.6.2. Linear and periodic models are fit to these lightcurves in chapter 6 and they are interpreted in chapter 7.

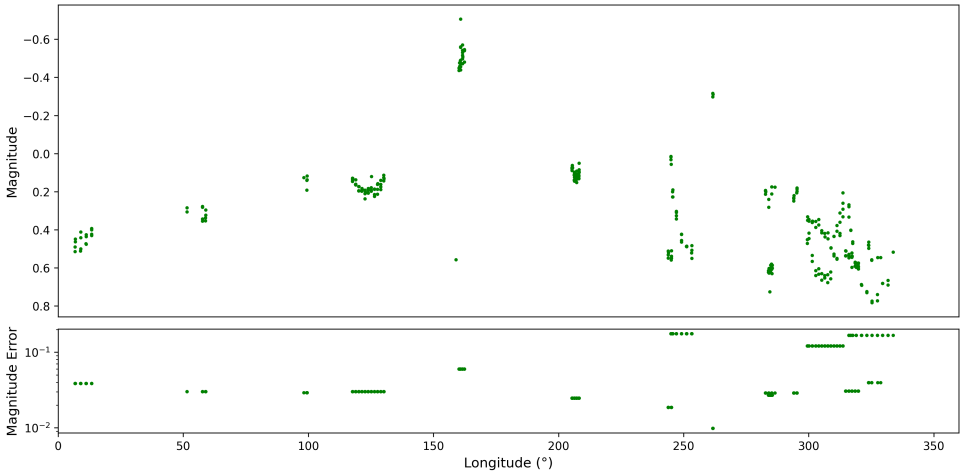

Figure 5-1: Titania's lightcurve in the Sloan g' filter

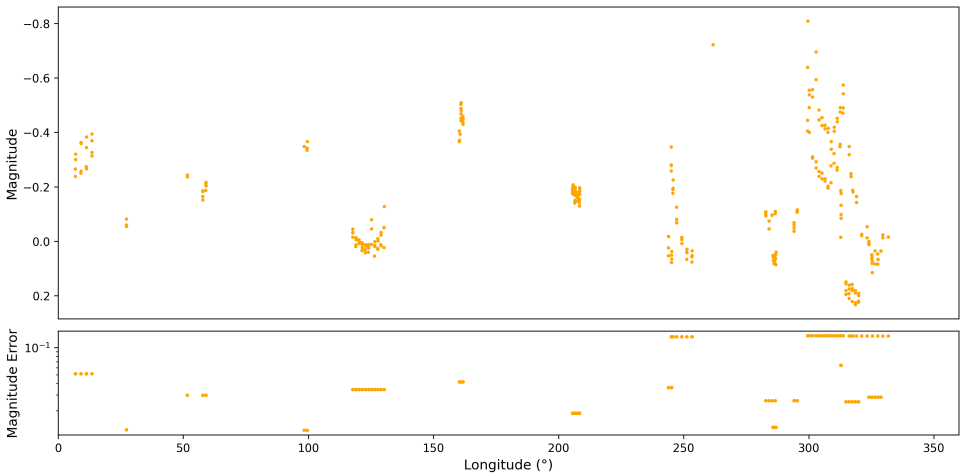

Figure 5-2: Titania's lightcurve in the Sloan r' filter

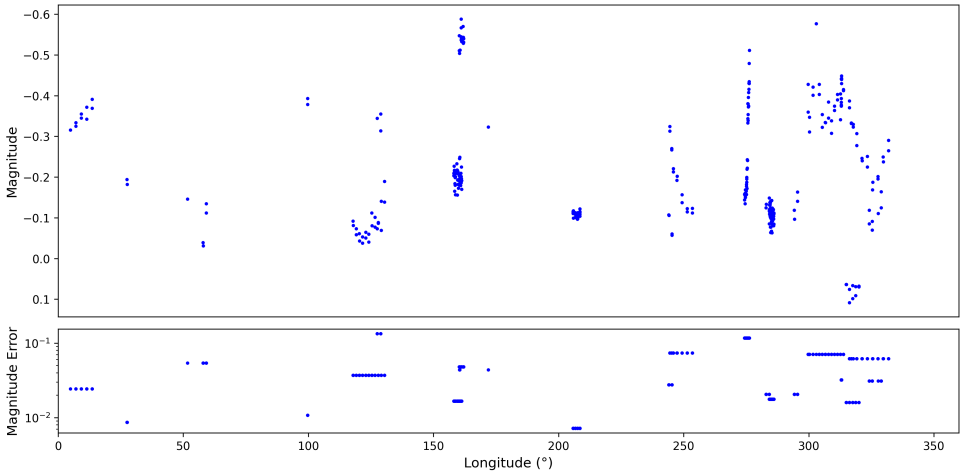

Figure 5-3: Titania's lightcurve in the Sloan i' filter

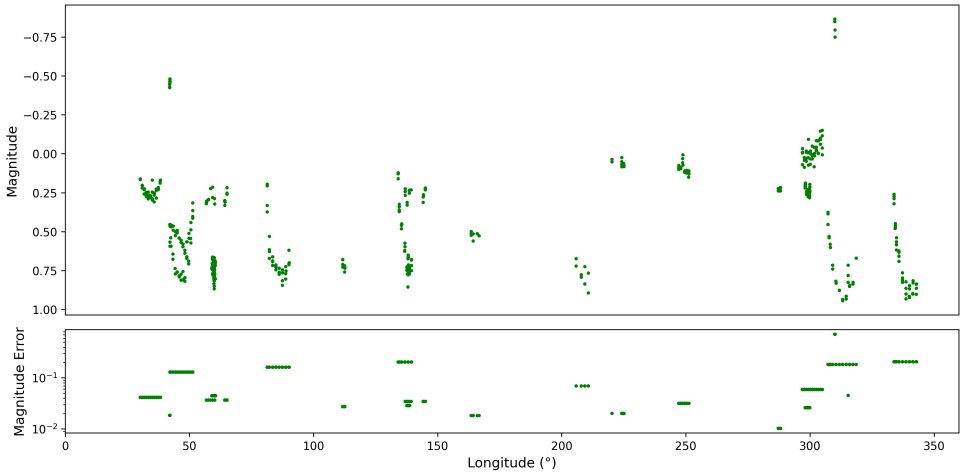

Figure 5-4: Oberon's lightcurve in the Sloan g' filter

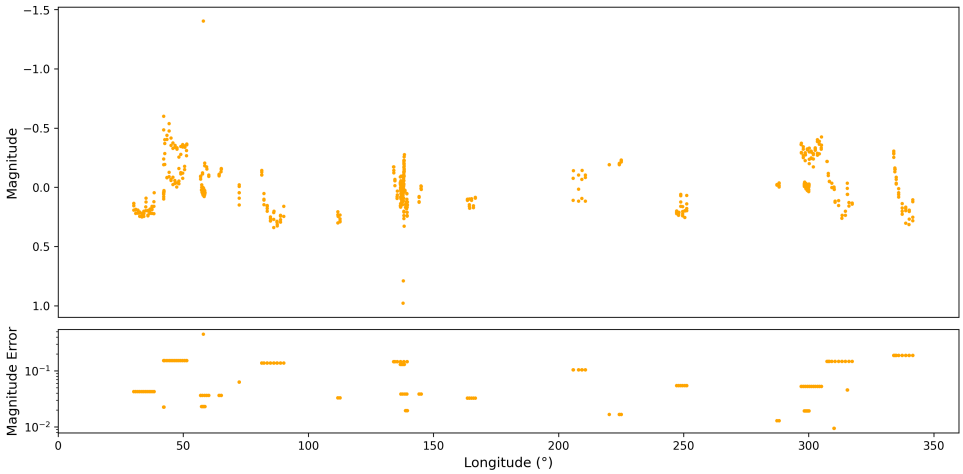

Figure 5-5: Oberon's lightcurve in the Sloan r' filter

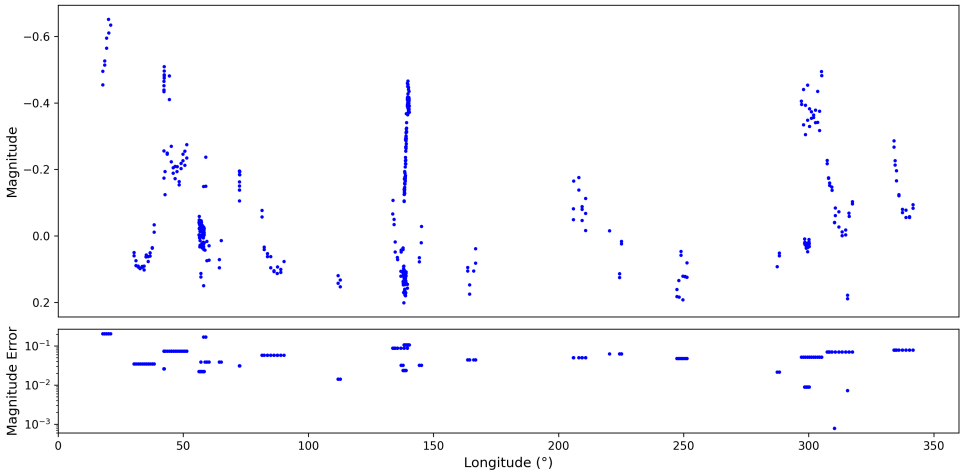

Figure 5-6: Oberon's lightcurve in the Sloan i' filter

Chapter 6

Model Fitting

6.1 Linear Models

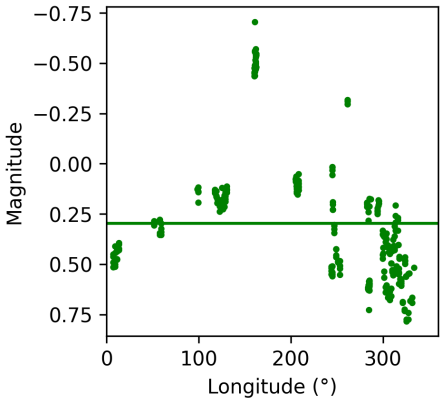

Figure 6-1: Best-fit horizontal line for Titania's g' lightcurve. The mean of the residuals from longtiude 75° - 275° is 0.183 magnitudes whereas the mean of the residuals from longitude 275° - 75° is -0.21 magnitudes. These differences indicate that Titania is not uniformly bright.

Non-uniform lightcurves are consistent with the Voyager 2 spacecraft images of Titania and Oberon figure 1-3. In the spacecraft images, there are clearly identifiable brighter regions and darker regions on both Titania and Oberon. In order a demonstrate the need for a periodic model, a linear model is fit to one of the lightcurves for each moon. It is expected that the lightcurves in different filters follow similar trends, so non-uniform brightness in one of the filters indicates that that the other filters could also have non-uniform brightness. The best-fit flat line for the g' Titania data and the and i' Oberon data are are plotted in this section. These filters were selected because the non-uniformity was apparent by eye. For the g' Titania data, the mean of the residuals from longitudes 75° - 275° is 0.183 magnitudes and the mean of the residuals from longitudes 275° - 75° is -0.21 magnitudes. For comparison, the standard deviation of the absolute value of the residuals

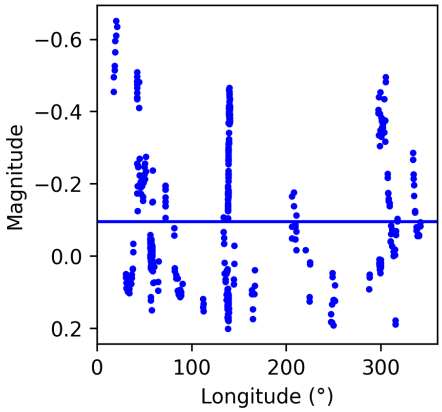

Figure 6-2: Best-fit horizontal line for Oberon's i' lightcurve. The mean of the residuals from longitude 25° - 300° is -0.11 magnitudes whereas the mean of the residuals from longitude 300° - 25° is 0.02 magnitudes. These differences indicate that Oberon is not uniformly bright.

0.19 magnitudes. For the i' Oberon data, the mean of the residuals from longitude 25° - 300° is -0.11 magnitudes and the mean of the residuals from longitude 300° - 25° is 0.02 magnitudes. For these data, the standard deviation of the absolute value of the residuals is 0.10 magnitudes. These differences indicate that Titania and Oberon are not uniformly bright and that more complex models should be considered. The lightcurves of Titania and Oberon in the Johnson V filter reported by (Goguen, Hammel, and Brown 1989) and reproduced in chapter 1.2 also find that the moons are not uniformly bright.

6.2 Periodic Models

Fourier transforms were fit to the data using scipy's curve fit function. Fourier transforms of first through sixth orders were fit to each lightcurve, and the results are plotted in this section. The period of the Fourier transforms were fixed to be 8.706 and and 13.46 days for Titania and Oberon respectively. As an example, the formula for a sixth order Fourier transform is given by

$$\begin{aligned} y = & a_0 + a_1 \cdot \cos(x) + b_1 \cdot \sin(x) \\ & + a_2 \cdot \cos(2x) + b_2 \cdot \sin(2x) \\ & + a_3 \cdot \cos(3x) + b_3 \cdot \sin(3x) \\ & + a_4 \cdot \cos(4x) + b_4 \cdot \sin(4x) \\ & + a_5 \cdot \cos(5x) + b_5 \cdot \sin(5x) \\ & + a_6 \cdot \cos(6x) + b_6 \cdot \sin(6x) \end{aligned} \tag{6.1}$$

The goodness of fit of the models was evaluated with the reduced χ^2 statistic. This statistic is given by

$$\chi^2_{\text{red}} = \frac{\chi^2}{n-k-1} \tag{6.2}$$

where

$$\chi^2 = \sum \frac{(x_i - \bar{x})^2}{\sigma^2}, \tag{6.3}$$

n is the number of data points and k is the number of parameters in the model. A reduced χ^2 value of about 1 indicates that the model fits well to the data. Many of the reduced χ^2 values are substantially higher than 1 due to the scatter in the data points. It is not possible for first through sixth orders of Fourier transforms to fit well to all of the data points. On all of the lightcurves, there is at least one cluster of points that requires the model to have large variations in amplitude on a relatively short time scale.

On Titania's g' lightcurve, there is a cluster of points near magnitude -0.4 which is significantly brighter than the surrounding points. The rest of the lightcurve does indicate that Titania is brighter in the mid-longitudes, but there are no other points as bright as magnitude -0.4. The trends in Titania's r' and i' data are much less clear than in Titania's g' data. On Titania's r' lightcurve, only the fourth and higher degree Fourier transforms fit well to the data points between 0° and 200° longitude. Even so, many of these clusters of data are fit with their own feature. While it is not impossible that Titania has high frequency variations in brightness, fitting these high frequency variations to the current data is likely to be overfitting. A model with features at each of these clusters of data points could be considered if additional observations were made and the lightcurve was sampled at a higher frequency. This lightcurve also has a spread of nearly 1 magnitude between longitudes of 300° - 350°. On Titania's i' lightcurve, even the sixth order Fourier transform does not reflect many of the variations in the data. As examples, near 175° longitude on Titania's i' lightcurve, there is a cluster of data points around magnitude -0.15 and around magnitude -0.55. Near 325° longitude, there is a cluster of data points around magnitude 0.1, and a cluster of data points near magnitude -0.35. Nearby, around 240° longitude there is another cluster of data points centered around magnitude -0.15. Again, there is no way for a low order Fourier transform to fit well to all of these groups of data points.

On Oberon's g' lightcurve there are clusters of data points around 25° longitude that span from magnitude 0.75 to magnitude -0.50. There are also data points from 300° - 350° longitude which span nearly 1.75 magnitudes. There is less variance on Oberon's r' lightcurve than on its g' lightcurve. The data points near 50° longitude span 0.5 magnitudes, but no other areas on the lightcurve have variance this large. While Oberon's i' lightcurve does show a clear drop in brightness in the mid-longitudes, there are still inconsistencies in some of the data points. Near 25° longitude, for example, the data are 0.5 magnitudes brighter than the first order Fourier transform model. In fact, this cluster of data is never less than 0.5 magnitudes away from the best-fit Fourier transform, even

for the higher order models. At 140° and 300° of longitude, the data points range from magnitude 0.2 to - 0.5.

Even though the reduced χ^2 values are not near 1, higher orders of Fourier transforms were not included in order to avoid overfitting the data. However, do note that the reduced χ^2 values of the higher order Fourier transforms are closer to 1 than the models reported here. As an example, the fourth and higher order Fourier transform is already overfitting the Titania g' data. Notice that the model identifies maxima and minima which are not represented in the data. Even the third order Fourier Transform indicates a minimum between 50° and 100° longitude which is not present in the data. The third order Fourier transform does fit better to the brightest -0.5 magnitude data points around 175° longitude than the lower the first and second order Fourier transforms do. In this case, a third order Fourier transform would be justified if we are confident that the brightest data points are accurate. Since this lightcurve also contains points which are as dim as 0.8 magnitudes, these brightest points indicate that Titania's brightness spans nearly 1.5 magnitudes. Excluding the brightest points at -0.5 magnitudes, the brightness would only range about 0.8 magnitudes. The data points at -0.5 magnitudes could be indicative of a highly localized, bright geologic feature. While such a feature is not impossible, it is more likely that these data points are the result of systematic error in the observations, such as contamination due to stray light from Uranus. Because such contamination could artificially increase the satellites brightness, the second order Fourier transform model is the most preferable.

A more quantitative way to select the order of the Fourier transform model that should be adopted is to evaluate how the reduced χ^2 values change as a function of the order of the model. Since there are many more data points than parameters in the models, the reduced χ^2 approaches 1 as the order of the Fourier transform increases because a higher order Fourier transform can fit higher frequency variations in the data than a lower order Fourier transform. The rate of change of the reduced χ^2 can be a good indicator. If the reduced χ^2 decreases relatively rapidly as the the order of the Fourier transform increases, it indicates the higher order terms should be included in the model. On the other hand, if the reduced χ^2 value decreases relatively slowly, higher order terms could be overfitting the data. A sharp change in the slope of the reduced χ^2 could imply that the optimal order has been found. This kind of sharp change does occur at order 5 for Titania's g' lightcurve. However, because this order is has maxima/minima that are not present in the data, we opt for a lower order Fourier transform. Oberon's g' lightcurve also has a sharp change, which occurs at order 2. The other lightcurves do not have a sharp change. Oberon's order 3 and higher Fourier transforms overfit and have a brighter magnitude than the data at 0° longitude. This is also true of the order 2 model, but to a lesser extent. The order 1 model doesn't appear to overfit in this way. Because it is expected that the lightcurves from the different filters have similar shapes, it is also expected that lightcurves should be fit with the same order Fourier transform. Based on all of

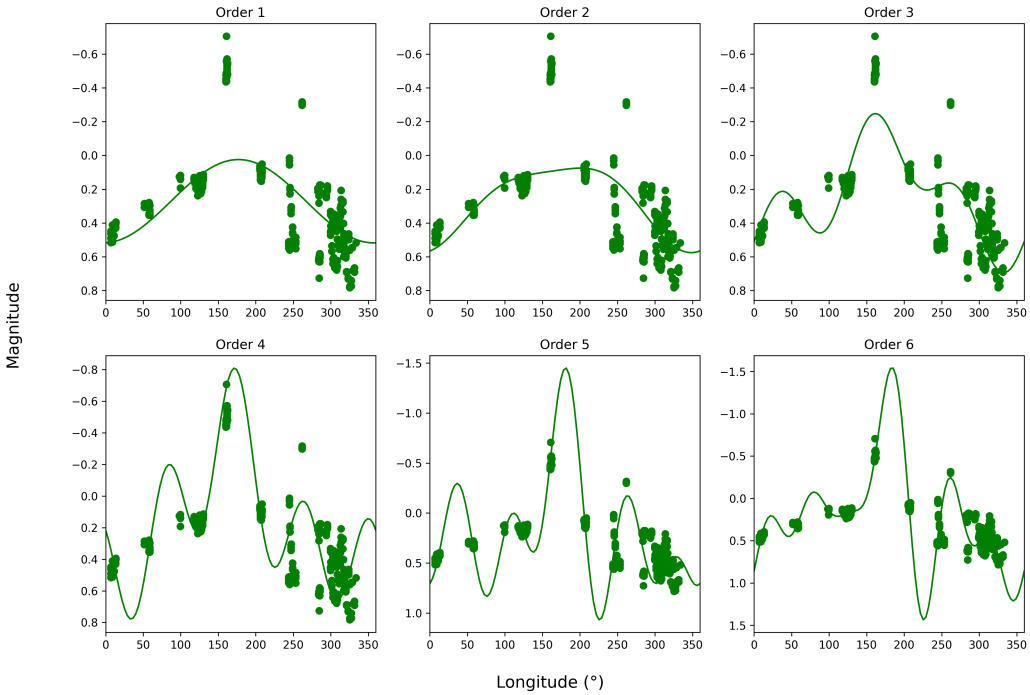

Figure 6-3: Periodic Models for Titania's g' lightcurve

the above, we adopt the following as our preferred light curve solutions: the Titania g' order 2 fit, Oberon r' order 2 fit, and Oberon i' order 2 fit. Other fits will be disregarded in further analysis.

Titania's g' best-fit model is:

$$y = 0.27 + 0.24 \cdot \cos(x) - 0.031 \cdot \sin(x) + 0.051 \cdot \cos(2x) - 0.032 \cdot \sin(2x) \tag{6.4}$$

Oberon's r' best-fit model is:

$$y = 0.015 + 0.031 \cdot \cos(x) + 0.096 \cdot \sin(x) + 0.041 \cdot \cos(2x) - 0.058 \cdot \sin(2x) \tag{6.5}$$

Oberon's i' best-fit model is:

$$y = -0.0024 - 0.098 \cdot \cos(x) + 0.012 \cdot \sin(x) - 0.074 \cdot \cos(2x) - 0.026 \cdot \sin(2x) \tag{6.6}$$

These three models will be used for analysis in the next chapter.

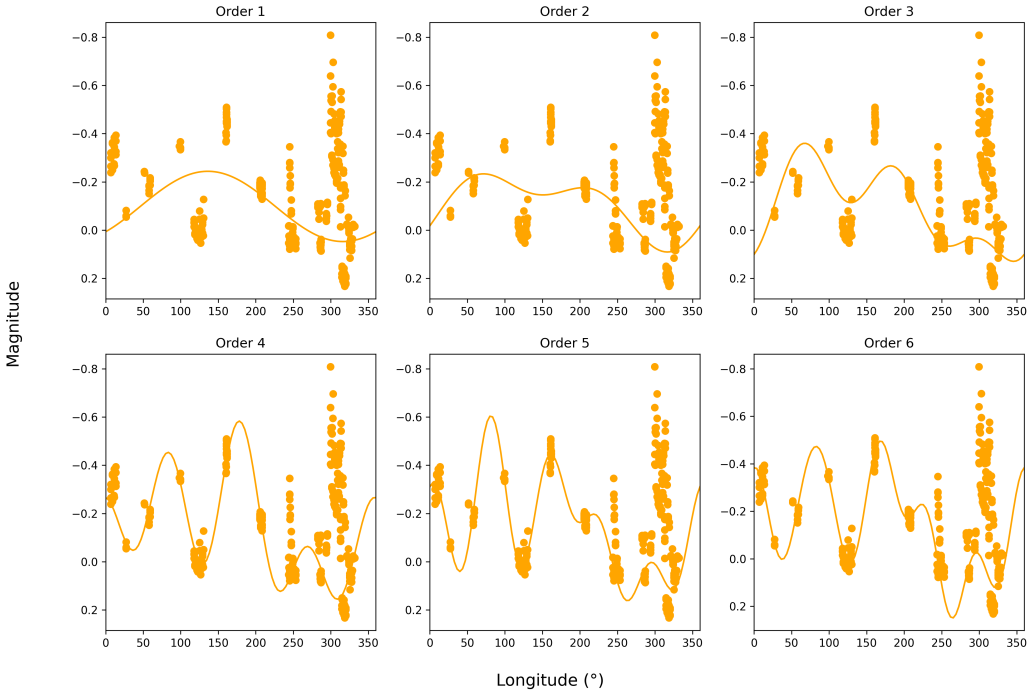

Figure 6-4: Periodic Models for Titania's r' lightcurve

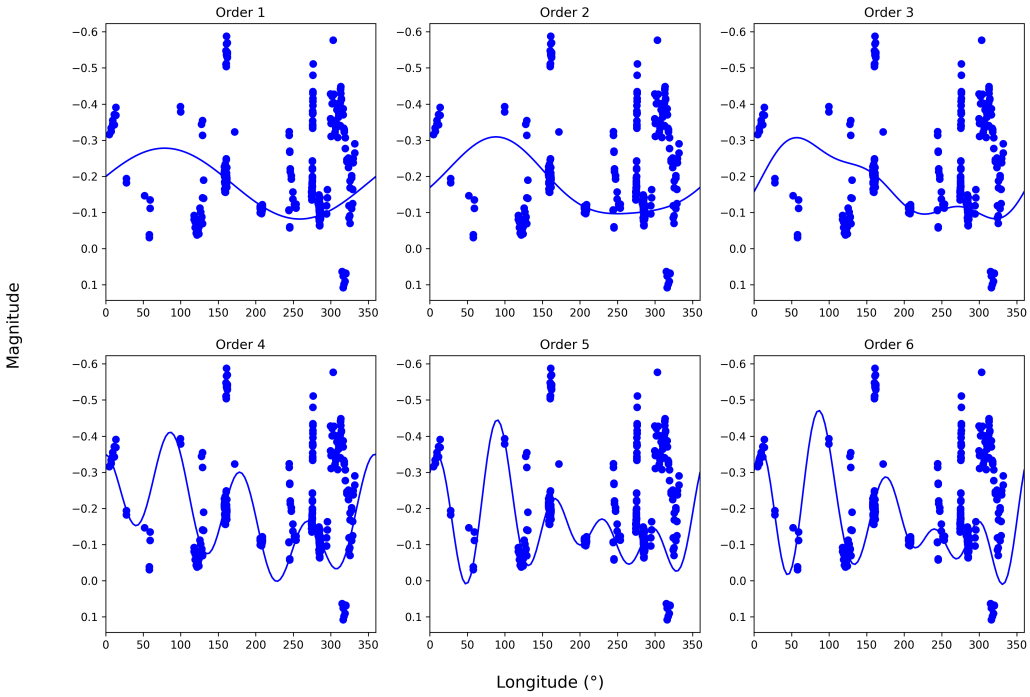

Figure 6-5: Periodic Models for Titania's i' lightcurve

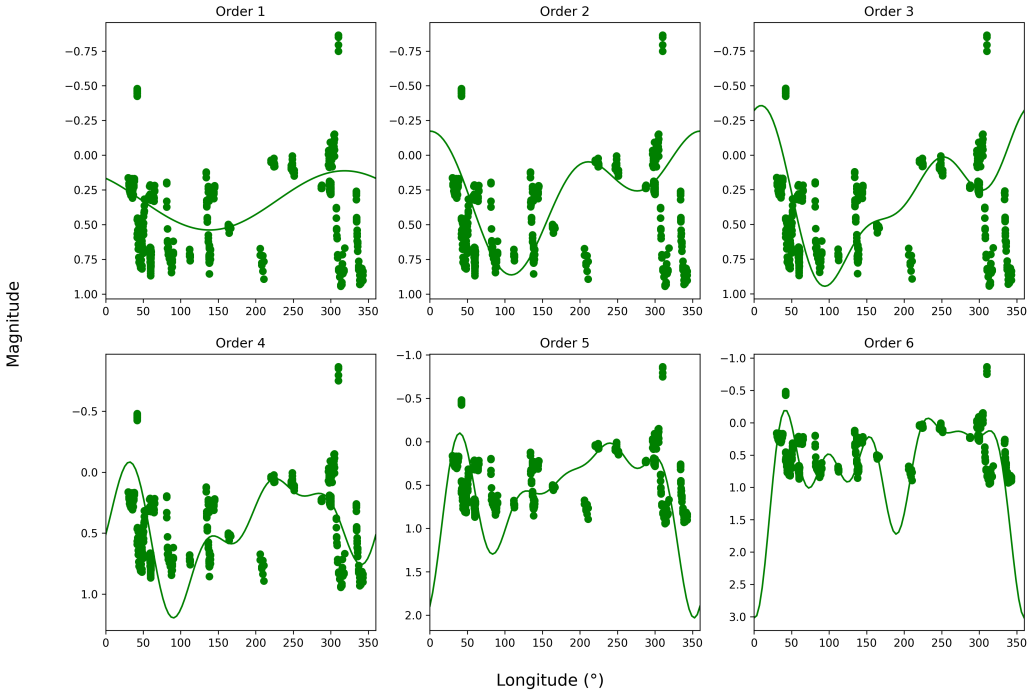

Figure 6-6: Periodic Models for Oberon's g' lightcurve

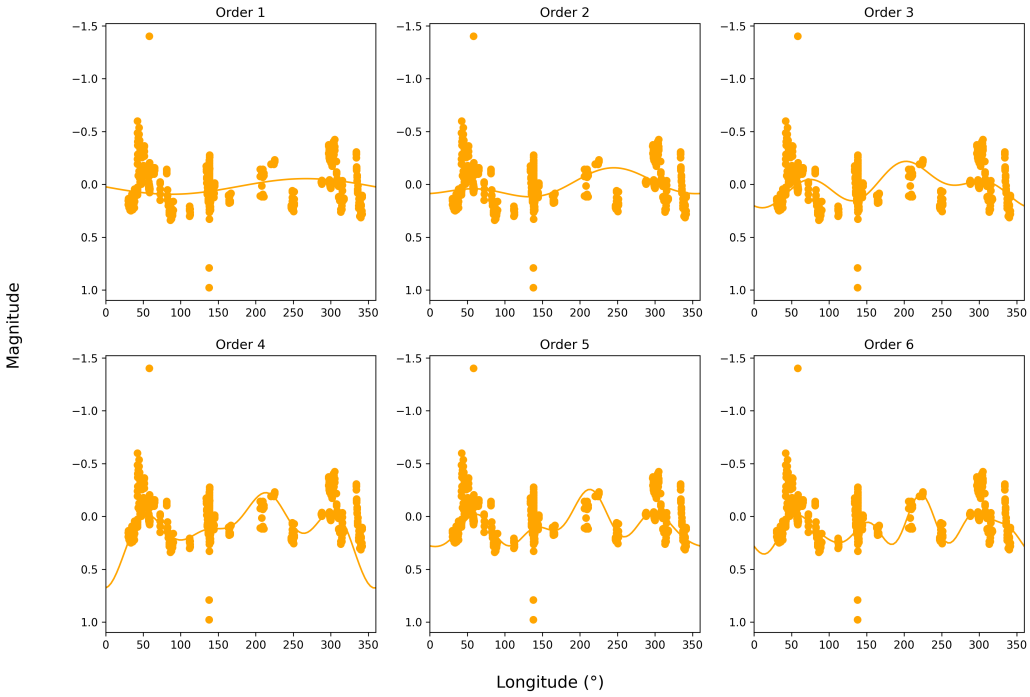

Figure 6-7: Periodic Models for Oberon's r' lightcurve

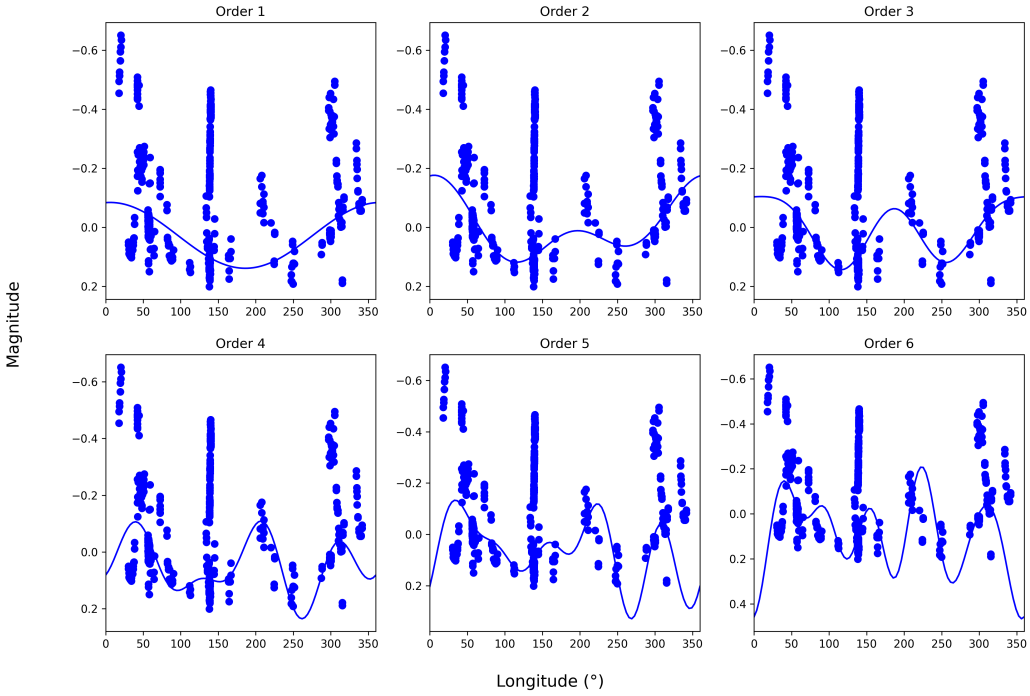

Figure 6-8: Periodic Models for Oberon's i' lightcurve

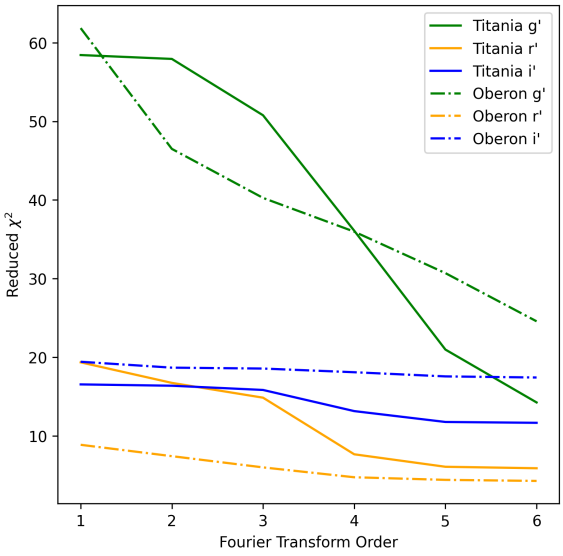

Figure 6-9: The reduced χ^2 as a function of Fourier transform order for each of the model lightcurves. A sharp change in the slope of the line could indicate the optimal order, but many of the lines do not have such a feature.

Chapter 7

Discussion

This section discusses the three best lightcurves, the Titania g', Oberon r', and Oberon i' lightcurves. These lightcurves were selected for the reasons outlined in chapter 6. The best-fit model for each of these lightcurves was a second order Fourier transform. Note that throughout this section the convention used in (R. J. Cartwright et al. 2015) and (Richard J. Cartwright, Emery, et al. 2018) will be adopted where the eastern or leading hemisphere refers to longitudes between 0° and 180° and the western or trailing hemisphere refers to longitudes between 180° and 360°. These lightcurves indicate that Titania's magnitude is singly periodic, with the mid-longitudes being the brightest. According to this model, Titania varies 0.49 magnitudes in brightness over the course of its period. It is the brightest at 201° longitude and the dimmest at 0° longitude, reaching magnitudes of 0.561 and 0.074 respectively. Oberon's r' lightcurve is doubly periodic. There are local extrema at 43° which has a magnitude of 0.003, 141° which has a magnitude of 0.165, 254° which has a magnitude of -0.134, and 352° which has a magnitude of 0.026. Thus, the eastern hemisphere is dimmer than the western hemisphere and has a smaller variation in magnitude. Oberon's i' lightcurve has extrema at 6° longitude where the magnitude is -0.176, 116° longitude where the magnitude is 0.117, 197° longitude where the magnitude is 0.012, and 260° longitude where the magnitude is 0.063.

These lightcurves suggest that the leading and trailing hemispheres of Oberon are more asymmetric than the hemispheres on Titania. While Titania is brighter at the mid-longitudes, there is not a clear distinction between the eastern and western hemispheres. The lightcurves also suggest that the trailing hemisphere of Oberon is brighter than the leading hemisphere, in both the r' and i' filters. Spectral observations taken from 2000 - 2013 indicate that both Titania and Oberon have asymmetric ice distributions, with more carbon dioxide ice on the trailing hemispheres and more water ice on the leading hemispheres (R. J. Cartwright et al. 2015). (R. J. Cartwright et al. 2015) also found that the abundance of carbon dioxide ice and the asymmetry in the water ice are less on the satellites that are farther away from Uranus. Only a slight asymmetry in the water ice was

detected on Oberon. Thus, the lightcurves presented here indicate that the asymmetries on Titania have lessened and the asymmetries on Oberon have become more extreme since 2013. These shifts could be due to several geologic processes. It is possible that new ice could have been deposited onto the mid-longitudes of Titania, causing that region to appear brighter. It is also possible that ice closer to 0° longitude has been weathered away. The asymmetry could be more extreme on Oberon because there is new surface ice on the western hemisphere or because the ice on the eastern hemisphere is being weathered away. It is also possible that changes in the ice distribution could be due to seasonal changes. Because of Uranus's extreme axial tilt, the northern and southern hemispheres of each moon experience long periods of light followed by long periods of darkness. Perhaps this variation has indirect effects that manifest as differences between the leading and trailing hemispheres. There could also be seasonality as the distance between the sun and Uranus varies across its orbit. However, Uranus has an 84 year orbital period, so variation as a result of Uranus's distance to the sun would likely occur over a roughly 42 year timescale. A longer term observing campaign would be required to confirm such a change. It has also been hypothesized that the asymmetry in the ice distributions is due to electron bombardment from Uranus's magnetic field. Thus, a change in the ice distribution could be reflective of a change in Uranus's magnetic field; however such a change is unlikely to have occurred. If so, it would require that the field has been weakened near Titania and strengthened near Oberon.

As shown in the lightcurves, on Oberon, r' is brighter than i' from 75° to 309° longitude with peaks at 90° and 257° longitude. Thus, Oberon is bluer between 75° and 309° longitude and redder between 309° and 75° longitude. It was previously reported that the leading hemispheres of Titania and Oberon are redder than the trailing hemispheres (Richard J. Cartwright, Emery, et al. 2018). Thus, these data imply that the relative colors on Oberon have changed and the leading and trailing hemispheres are no longer clearly split between red and blue.

As described in section 1.2, the only reported lightcurves of Titania and Oberon are the Johnson V ones in (Goguen, Hammel, and Brown 1989). It is difficult to identify a trend in (Goguen, Hammel, and Brown 1989's) Titania lightcurve, but the data points tend to be within 0.2 magnitudes of each other. This is a significantly smaller variation than the 0.49 magnitude variation reported here. 0.5 magnitudes of variation is quite extreme and requires that there is a large range of materials on the surface. (Goguen, Hammel, and Brown 1989) reports a similar 0.2 magnitude variation in the Johnson V lightcurve for Oberon. The 0.3 magnitude variation indicated in both Oberon's r' and i' lightcurves reported here are more consistent with (Goguen, Hammel, and Brown 1989). Oberon's lightcurve in (Goguen, Hammel, and Brown 1989) is clearly non-uniform and appears to be singly periodic. This could be consistent with the r' and i' lightcurves reported here, but it is difficult to compare the data because the lightcurves reported by (Goguen, Hammel, and Brown 1989) are plotted as a function of the Fraction of the Period as opposed to the longitude. Comparisons are

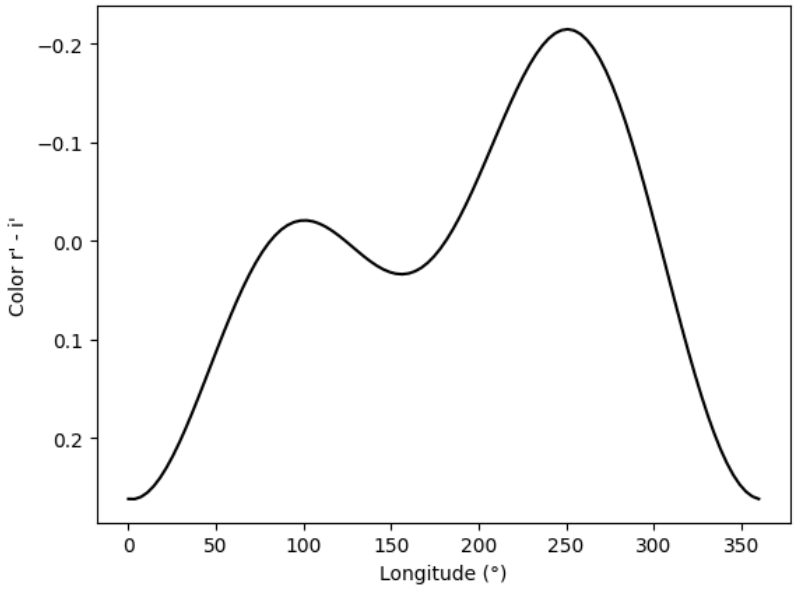

Figure 7-1: The model Oberon's i' lightcurve subtracted from the model of Oberon's r' lightcurve

also difficult because the lightcurves are in different filters.

Chapter 8

Conclusion

8.1 Future Work

The surface features discovered by Voyager 2 indicate the need for a long-term program which makes photometric measurements of the satellites over time. However, no such program exists. The comparison of a current day lightcurve to a previous one can be used to determine if/how the surface properties of the satellites are changing over time. In the future, the observations reported here could form the basis for a long-term program which makes ongoing photometric measurements of the Uranian satellites. Small ground-based telescopes, such as those at MIT's Wallace Observatory, could be good candidates for such a program. A long-term program is particularly useful due to the satellites' extreme seasonal cycles. The moons are in the dark for 42 years before being in the light for 42 years, which could lead to variations in surface properties on decadal timescales. More involved photometric techniques, such as PSF and differential photometry, and larger telescopes would be useful for better resolving the moons and Uranus. These could also improve the accuracy of the photometry by removing contamination due to diffraction spikes and saturation. More involved techniques are especially important for the inner satellites, which are more affected by this contamination than the outer satellites.

8.2 Broader Implications

Knowledge of the Uranian system has several implications for the study of other bodies within the Solar System and beyond. For example, it is hypothesized the major Uranian satellites could contain subsurface oceans (Richard J. Cartwright, Beddingfield, et al. 2021). Not only does this have implications for their habitability, subsurface oceans on the Uranian satellites could be a useful comparison to better interpret the results of upcoming missions to ocean worlds, namely the Europa

Clipper mission. Moreover, the major Uranian satellites' surface ices are of common composition to those in the Pluto-Charon system, however, a further investigation could give insight into an icy evolution very different than those of Kuiper Belt Objects (Cohen et al. 2022). Investigation of the Uranian system also has implications for exoplanet studies; Uranus could be used to indirectly study Uranus-like exoplanets whose characteristics cannot be observed in detail. Additionally, understanding the formation and evolution of the Uranian system is necessary for understanding the formation and evolution of the Solar System. For instance, it is theorized that Uranus could have undergone significant migration which would have dynamically impacted other objects. The diversity of Uranus's moons, which range from primitive to captured asteroids, provide a unique opportunity to study a range of formation and evolution processes which is applicable to other satellite systems in the Solar System and beyond.

Chapter 9

Appendix

Date	Telescope	Num	Identifier	Calib Star RA	Calib Star Dec	g mag	g mag err	r mag	r mag err	i mag	i mag err
20231101	Elliot	C1	199211	03 15 18.32	17 54 27.2520	10.271	0.237	9.033	0.039	8.576	0.059
20231101	Elliot	C2	185098	03 15 25.88	17 35 42.2593	11.404	0.04	10.228	0.06	9.654	0.034
20231101	Elliot	C3	185254	3 15 53.43098	17 50 13.2181	11.244	0.036	10.827	0.01	10.634	0.108
20231102	Elliot	C1	199211	03 15 18.32159	17 54 27.2520	10.271	0.237	9.033	0.039	8.576	0.059
20231102	Elliot	C2	185098	03 15 25.88402	17 35 42.2593	11.404	0.04	10.228	0.06	9.654	0.034
20231102	Elliot	C3	185254	3 15 53.43098	17 50 13.2181	11.244	0.036	10.827	0.01	10.634	0.108
20231107	Elliot	C1	199211	03 15 18.32159	17 54 27.2520	10.271	0.237	9.033	0.039	8.576	0.059
20231107	Elliot	C2	199246	03 13 58.82881	17 53 19.2372	9.649	0.604	9.295	0.027	9.329	0
20231107	Elliot	C3	184739	03 14 08.85000	17 33 27.7742	12.028	0.049	11.161	0.006	10.877	0.054
20231111	Elliot	C1	199211	03 15 18.32159	17 54 27.2520	10.271	0.237	9.033	0.039	8.576	0.059
20231111	Elliot	C2	199246	03 13 58.82881	17 53 19.2372	9.649	0.604	9.295	0.027	9.329	0
20231111	Elliot	C3	184739	03 14 08.85000	17 33 27.7742	12.028	0.049	11.161	0.006	10.877	0.054
20231112	Elliot	C1	199211	03 15 18.32159	17 54 27.2520	10.271	0.237	9.033	0.039	8.576	0.059
20231112	Elliot	C2	199246	03 13 58.82881	17 53 19.2372	9.649	0.604	9.295	0.027	9.329	0
20231112	Elliot	C3	184739	03 14 08.85000	17 33 27.7742	12.028	0.049	11.161	0.006	10.877	0.054
20231115	Elliot	C1	198955	03 12 57.78311	17 43 27.7934	11.449	0.04	10.483	0.03	10.147	0.035
20231115	Elliot	C2	198901	03 13 15.20782	17 35 35.7576	11.192	0.048	10.706	0.02	10.577	0.004
20231115	Elliot	C3	198920	03 12 17.29826	17 32 27.2726	12.22	0.029	11.743	0.006	11.597	0.038
20231116	Elliot	C1	198955	03 12 57.78311	17 43 27.7934	11.449	0.04	10.483	0.03	10.147	0.035
20231116	Elliot	C2	198901	03 13 15.20782	17 35 35.7576	11.192	0.048	10.706	0.02	10.577	0.004
20231116	Elliot	C3	198920	03 12 17.29826	17 32 27.2726	12.22	0.029	11.743	0.006	11.597	0.038
2023116	P2	C1	198955	03 12 57.78311	17 43 27.7934	11.449	0.04	10.483	0.03	10.147	0.035
2023116	P2	C2	198901	03 13 15.20782	17 35 35.7576	11.192	0.048	10.706	0.02	10.577	0.004

Table 9.1 continued from previous page

Date	Telescope	Num	Identifier	Calib Star RA	Calib Star Dec	g mag	g mag err	r mag	r mag err	i mag	i mag err
20231116	P2	C3	198920	03 12 17.29826	17 32 27.2726	12.22	0.029	11.743	0.006	11.597	0.038
20231116	P3	C1	198955	03 12 57.78311	17 43 27.7934	11.449	0.04	10.483	0.03	10.147	0.035
20231116	P3	C2	198901	03 13 15.20782	17 35 35.7576	11.192	0.048	10.706	0.02	10.577	0.004
20231116	P3	C3	198920	03 12 17.29826	17 32 27.2726	12.22	0.029	11.743	0.006	11.597	0.038
20231118	Elliot	C1	198955	03 12 57.78311	17 43 27.7934	11.449	0.04	10.483	0.03	10.147	0.035
20231118	Elliot	C2	198901	03 13 15.20782	17 35 35.7576	11.192	0.048	10.706	0.02	10.577	0.004
20231118	Elliot	C3	198920	03 12 17.29826	17 32 27.2726	12.22	0.029	11.743	0.006	11.597	0.038
20231118	P2	C1	198878	03 12 39.15070	17 28 06.9781	11.685	0.042	11.29	0.013	11.159	0.006
20231118	P2	C2	198901	03 13 15.20782	17 35 35.7576	11.192	0.048	10.706	0.02	10.577	0.004
20231118	P2	C3	198920	03 12 17.29826	17 32 27.2726	12.22	0.029	11.743	0.006	11.597	0.038
20231118	P3	C1	198955	03 12 57.78311	17 43 27.7934	11.449	0.04	10.483	0.03	10.147	0.035
20231118	P3	C2	198878	03 12 39.15070	17 28 06.9781	11.685	0.042	11.29	0.013	11.159	0.006
20231118	P3	C3	198920	03 12 17.29826	17 32 27.2726	12.22	0.029	11.743	0.006	11.597	0.038
20231127	Elliot	C1	198807	03 11 04.81270	17 18 15.0013	9.339	0.981	8.383	0	8.337	0.007
20231127	Elliot	C2	198791	03 11 37.84727	17 19 37.4232	11.457	0.012	10.503	0.035	10.201	0.057
20231127	Elliot	C3	198838	03 11 50.95081	17 24 49.0822	11.37	0.031	11.005	0.008	10.906	0.017
20231128	Elliot	C1	198807	03 11 04.81270	17 18 15.0013	9.339	0.981	8.383	0	8.337	0.007
20231128	Elliot	C2	198791	03 11 37.84727	17 19 37.4232	11.457	0.012	10.503	0.035	10.201	0.057
20231128	Elliot	C3	198838	03 11 50.95081	17 24 49.0822	11.37	0.031	11.005	0.008	10.906	0.017
20231206	P2	C1	198990	03 09 38.25817	17 27 47.6280	12.527	0	11.612	0	11.181	0
20231206	P2	C2	199001	03 09 24.06481	17 30 38.5165	12.852	0	12.323	0	12.071	0.024
20231206	P2	C3	198814	03 10 17.80632	17 16 44.1010	13.558	0.008	12.362	0.01	11.864	0.026

Table 9.1 continued from previous page

Date	Telescope	Num	Identifier	Calib Star RA	Calib Star Dec	g mag	g mag err	r mag	r mag err	i mag	i mag err
20231206	P3	C1	198990	03 09 38.25817	17 27 47.6280	12.527	0	11.612	0	11.181	0
20231206	P3	C2	199001	03 09 24.06481	17 30 38.5165	12.852	0	12.323	0	12.071	0.024
20231206	P3	C3	198814	03 10 17.80632	17 16 44.1010	13.558	0.008	12.362	0.01	11.864	0.026
20231207	Elliot	C1	198990	03 09 38.25817	17 27 47.6280	12.527	0	11.612	0	11.181	0
20231207	Elliot	C2	199001	03 09 24.06481	17 30 38.5165	12.852	0	12.323	0	12.071	0.024
20231207	Elliot	C3	198814	03 10 17.80632	17 16 44.1010	13.558	0.008	12.362	0.01	11.864	0.026
20231208	Elliot	C1	198990	03 09 38.25817	17 27 47.6280	12.527	0	11.612	0	11.181	0
20231208	Elliot	C2	199001	03 09 24.06481	17 30 38.5165	12.852	0	12.323	0	12.071	0.024
20231208	Elliot	C3	198814	03 10 17.80632	17 16 44.1010	13.558	0.008	12.362	0.01	11.864	0.026
20231211	Elliot	C1	97054	03 09 18.14976	17 14 19.8887	14.363	0.038	13.575	0.016	13.233	0.072
20231211	Elliot	C2	97074	03 09 00.70461	17 21 23.1190	13.145	0.049	12.795	0.039	12.704	0.043
20231211	Elliot	C3	198986	03 09 35.94624	17 26 43.6451	13.061	0	12.153	0	11.758	0.051
20231212	Elliot	C1	97054	03 09 18.14976	17 14 19.8887	14.363	0.038	13.575	0.016	13.233	0.072
20231212	Elliot	C2	97074	03 09 00.70461	17 21 23.1190	13.145	0.049	12.795	0.039	12.704	0.043
20231212	Elliot	C3	97119	03 08 17.25454	17 22 04.1843	13.787	0.014	13.331	0.005	13.133	0.05
20231212	P2	C1	97054	03 09 18.14976	17 14 19.8887	14.363	0.038	13.575	0.016	13.233	0.072
20231212	P2	C2	97074	03 09 00.70461	17 21 23.1190	13.145	0.049	12.795	0.039	12.704	0.043
20231212	P2	C3	97119	03 08 17.25454	17 22 04.1843	13.787	0.014	13.331	0.005	13.133	0.05
20231212	P3	C1	97054	03 09 18.14976	17 14 19.8887	14.363	0.038	13.575	0.016	13.233	0.072
20231212	P3	C2	97074	03 09 00.70461	17 21 23.1190	13.145	0.049	12.795	0.039	12.704	0.043
20231212	P3	C3	97119	03 08 17.25454	17 22 04.1843	13.787	0.014	13.331	0.005	13.133	0.05
20231214	Elliot	C1	97054	03 09 18.14976	17 14 19.8887	14.363	0.038	13.575	0.016	13.233	0.072

Table 9.1 continued from previous page

Date	Telescope	Num	Identifier	Calib Star RA	Calib Star Dec	g mag	g mag err	r mag	r mag err	i mag	i mag err
20231214	Elliot	C2	97074	03 09 00.70461	17 21 23.1190	13.145	0.049	12.795	0.039	12.704	0.043
20231214	Elliot	C3	97119	03 08 17.25454	17 22 04.1843	13.787	0.014	13.331	0.005	13.133	0.05
20231215	Elliot	C1	97054	03 09 18.14976	17 14 19.8887	14.363	0.038	13.575	0.016	13.233	0.072
20231215	Elliot	C2	97074	03 09 00.70461	17 21 23.1190	13.145	0.049	12.795	0.039	12.704	0.043
20231215	Elliot	C3	97119	03 08 17.25454	17 22 04.1843	13.787	0.014	13.331	0.005	13.133	0.05
20231215	P2	C1	97092	03 07 58.57801	17 19 03.5686	14.282	0.03	13.765	0.02	13.534	0.145
20231215	P2	C2	97119	03 08 17.25454	17 22 04.1843	13.787	0.014	13.331	0.005	13.133	0.05
20231215	P2	C3	97117	03 08 37.00178	17 21 55.6381	15.002	0.01	14.444	0	14.207	0.043
20231215	P3	C1	97092	03 07 58.57801	17 19 03.5686	14.282	0.03	13.765	0.02	13.534	0.145
20231215	P3	C2	97119	03 08 17.25454	17 22 04.1843	13.787	0.014	13.331	0.005	13.133	0.05
20231215	P3	C3	97117	03 08 37.00178	17 21 55.6381	15.002	0.01	14.444	0	14.207	0.043
20231216	Elliot	C1	97054	03 09 18.14976	17 14 19.8887	14.363	0.038	13.575	0.016	13.233	0.072
20231216	Elliot	C2	97074	03 09 00.70461	17 21 23.1190	13.145	0.049	12.795	0.039	12.704	0.043
20231216	Elliot	C3	97119	03 08 17.25454	17 22 04.1843	13.787	0.014	13.331	0.005	13.133	0.05
20231218	Elliot	C1	97054	03 09 18.14976	17 14 19.8887	14.363	0.038	13.575	0.016	13.233	0.072
20231218	Elliot	C2	97074	03 09 00.70461	17 21 23.1190	13.145	0.049	12.795	0.039	12.704	0.043
20231218	Elliot	C3	97119	03 08 17.25454	17 22 04.1843	13.787	0.014	13.331	0.005	13.133	0.05
20231219	Elliot	C1	97054	03 09 18.14976	17 14 19.8887	14.363	0.038	13.575	0.016	13.233	0.072
20231219	Elliot	C2	97074	03 09 00.70461	17 21 23.1190	13.145	0.049	12.795	0.039	12.704	0.043
20231219	Elliot	C3	97119	03 08 17.25454	17 22 04.1843	13.787	0.014	13.331	0.005	13.133	0.05
20231220	Ellliot	C1	96976	03 07 24.81291	17 04 23.5706	9.603	0.039	9.469	0.026	9.497	0.067
20231220	Elliot	C2	97094	03 07 19.53529	17 14 24.7596	12.441	0.017	11.684	0.07	11.321	0.009

Table 9.1 continued from previous page

Date	Telescope	Num	Identifier	Calib Star RA	Calib Star Dec	g mag	g mag err	r mag	r mag err	i mag	i mag err
20231220	Elliot	C3	97119	03 08 17.25454	17 22 04.1843	13.787	0.014	13.331	0.005	13.133	0.05
20231221	Elliot	C1	96976	03 07 24.81291	17 04 23.5706	9.603	0.039	9.469	0.026	9.497	0.067
20231221	Elliot	C2	97094	03 07 19.53529	17 14 24.7596	12.441	0.017	11.684	0.07	11.321	0.009
20231221	Elliot	C3	97119	03 08 17.25454	17 22 04.1843	13.787	0.014	13.331	0.005	13.133	0.05
20240104	Elliot	C1	97642	03 06 18.43054	17 06 57.6036	10.572	0.138	9.512	0.01	9.104	0.029
20240104	Elliot	C2	97674	03 06 15.18551	17 14 37.4999	11.323	0.026	10.934	0.023	10.798	0.045
20240104	Elliot	C3	97658	03 05 44.41343	17 09 57.9601	11.774	0.012	11.231	0.01	11.049	0.077
20240105	Elliot	C1	97642	03 06 18.43054	17 06 57.6036	10.572	0.138	9.512	0.01	9.104	0.029
20240105	Elliot	C2	97674	03 06 15.18551	17 14 37.4999	11.323	0.026	10.934	0.023	10.798	0.045
20240205	Elliot	C3	97658	03 05 44.41343	17 09 57.9601	11.774	0.012	11.231	0.01	11.049	0.077
20240114	TCS	C1	97651	03 05 32.26822	17 07 11.7910	11.443	0.02	10.975	0.08	10.788	0.01
20240114	TCS	C2	97644	03 05 50.41512	17 06 56.5595	12.371	0.006	11.973	0	11.903	0.087
20240116	Artemis	C1	97658	03 05 44.41343	17 09 57.9601	11.774	0.012	11.231	0.01	11.049	0.077
20240116	Artemis	C2	97651	03 05 32.26822	17 07 11.7910	11.443	0.016	10.951	0.067	10.768	0.031
20240116	Artemis	C3	97644	03 05 50.41512	17 06 56.5595	12.371	0.006	11.973	0	11.903	0.087
20240117	Elliot	C1	97658	03 05 44.41343	17 09 57.9601	11.774	0.012	11.231	0.01	11.049	0.077
20240117	Elliot	C2	97651	03 05 32.26822	17 07 11.7910	11.443	0.016	10.951	0.067	10.768	0.031
20240117	Elliot	C3	97635	03 05 33.54864	17 02 17.1746	13.4	0.015	13.141	0.261	12.804	0.043
20240121	TCS	C1	97651	03 05 32.26822	17 07 11.7910	11.443	0.02	10.975	0.08	10.788	0.01

Table 9.1 continued from previous page

Date	Telescope	Num	Identifier	Calib Star RA	Calib Star Dec	g mag	g mag err	r mag	r mag err	i mag	i mag err

Table 9.1: A list of the calibration stars used for photometric analysis on each night. All information presented here reflects values reported in the APASS catalog. Three stars were selected for each image, except when there were not three stars in the field. Note that APASS reports the error bars for some of these stars as 0, but that means that the error bar is not known. The identifier column lists the APASS catalog's reference number for that star.

Bibliography

Astropy Collaboration et al. (Aug. 2022). "The Astropy Project: Sustaining and Growing a Community-oriented Open-source Project and the Latest Major Release (v5.0) of the Core Package". In: 935.2, 167, p. 167. DOI: 10.3847/1538-4357/ac7c74. arXiv: 2206.14220 [astro-ph.IM].

Avramchuk, V. V., V. K. Rosenbush, and T. P. Bul'Ba (June 2007). "Photometric study of the major satellites of Uranus". In: *Solar System Research* 41.3, pp. 186–202. DOI: 10.1134/S0038094607030021.

Bradley, Larry et al. (May 2023). *astropy/photutils: 1.8.0*. Version 1.8.0. DOI: 10.5281/zenodo.7946442. URL: https://doi.org/10.5281/zenodo.7946442.

Cartwright, R. J. et al. (Sept. 2015). "Distribution of CO_2 ice on the large moons of Uranus and evidence for compositional stratification of their near-surfaces". In: *Icarus* 257, pp. 428–456. DOI: 10.1016/j.icarus.2015.05.020. arXiv: 1506.04673 [astro-ph.EP].

Cartwright, Richard J., Chloe B. Beddingfield, et al. (June 2021). "The Science Case for Spacecraft Exploration of the Uranian Satellites: Candidate Ocean Worlds in an Ice Giant System". In: *PSJ* 2.3, 120, p. 120. DOI: 10.3847/PSJ/abfe12. arXiv: 2105.01164 [astro-ph.EP].

Cartwright, Richard J., Joshua P. Emery, et al. (Nov. 2018). "Red material on the large moons of Uranus: Dust from the irregular satellites?" In: *Icarus* 314, pp. 210–231. DOI: 10.1016/j.icarus.2018.06.004. arXiv: 1806.01809 [astro-ph.EP].

Cohen, Ian J. et al. (Mar. 2022). "The Case for a New Frontiers-Class Uranus Orbiter: System Science at an Underexplored and Unique World with a Mid-scale Mission". In: *PSJ* 3.3, 58, p. 58. DOI: 10.3847/PSJ/ac5113.

DeColibus, Riley A., Nancy J. Chanover, and Richard J. Cartwright (Oct. 2023). "Are NH_3 and CO_2 Ice Present on Miranda?" In: *PSJ* 4.10, 191, p. 191. DOI: 10.3847/PSJ/acf834. arXiv: 2309.04844 [astro-ph.EP].

Detre, Ö. H. et al. (Sept. 2020). "Herschel-PACS photometry of the five major moons of Uranus". In: *A&A* 641, A76, A76. DOI: 10.1051/0004-6361/202037625. arXiv: 2006.09795 [astro-ph.EP].

Goguen, J. D., H. B. Hammel, and R. H. Brown (Feb. 1989). "V photometry of Titania, Oberon, and Triton". In: *Icarus* 77.2, pp. 239–247. DOI: 10.1016/0019-1035(89)90088-2.

Grundy, W. M. et al. (Oct. 2006). "Distributions of H $_2$O and CO $_2$ ices on Ariel, Umbriel, Titania, and Oberon from IRTF/SpeX observations". In: *Icarus* 184.2, pp. 543–555. DOI: 10.1016/j.icarus.2006.04.016.

Harris, Charles R. et al. (Sept. 2020). "Array programming with NumPy". In: *Nature* 585.7825, pp. 357–362. DOI: 10.1038/s41586-020-2649-2. URL: https://doi.org/10.1038/s41586-020-2649-2.

Henden, A. A. et al. (Jan. 2016). *VizieR Online Data Catalog: AAVSO Photometric All Sky Survey (APASS) DR9 (Henden+, 2016).*

Hunter, J. D. (2007). "Matplotlib: A 2D graphics environment". In: *Computing in Science & Engineering* 9.3, pp. 90–95. DOI: 10.1109/MCSE.2007.55.

Mallama, Anthony, Bruce Krobusek, and Hristo Pavlov (Jan. 2017). "Comprehensive wide-band magnitudes and albedos for the planets, with applications to exo-planets and Planet Nine". In: *Icarus* 282, pp. 19–33. DOI: 10.1016/j.icarus.2016.09.023. arXiv: 1609.05048 [astro-ph.EP].

team, The pandas development (Feb. 2020). *pandas-dev/pandas: Pandas*. Version latest. DOI: 10.5281/zenodo.3509134. URL: https://doi.org/10.5281/zenodo.3509134.

Virtanen, Pauli et al. (2020). "SciPy 1.0: Fundamental Algorithms for Scientific Computing in Python". In: *Nature Methods* 17, pp. 261–272. DOI: 10.1038/s41592-019-0686-2.